

UNCLASSIFIED

AD-A208 626

REPORT DOCUMENTATION PAGE

(2)

UNCLASSIFIED			1b. RESTRICTIVE MARKINGS									
2a. SECURITY CLASSIFICATION AUTHORITY			3. DISTRIBUTION / AVAILABILITY OF REPORT									
2b. DECLASSIFICATION / DOWNGRADING SCHEDULE			Approved for public release; distribution is unlimited.									
4. PERFORMING ORGANIZATION REPORT NUMBER(S)			5. MONITORING ORGANIZATION REPORT NUMBER(S)									
6a. NAME OF PERFORMING ORGANIZATION			7a. NAME OF MONITORING ORGANIZATION									
Univ of New Mexico			AFOSR/NP									
6c. ADDRESS (City, State, and ZIP Code)			7b. ADDRESS (City, State, and ZIP Code)									
Albuquerque, NM 87131			Building 410, Bolling AFB DC 20332-6448									
8a. NAME OF FUNDING / SPONSORING ORGANIZATION		8b. OFFICE SYMBOL (if applicable)	9. PROCUREMENT INSTRUMENT IDENTIFICATION NUMBER									
AFOSR		NP	AFOSR-86-0063									
8c. ADDRESS (City, State, and ZIP Code)			10. SOURCE OF FUNDING NUMBERS									
Building 410, Bolling AFB DC 20332-6448			<table border="1"> <tr> <th>PROGRAM ELEMENT NO.</th> <th>PROJECT NO.</th> <th>TASK NO.</th> <th>WORK UNIT ACCESSION NO.</th> </tr> <tr> <td>61102F</td> <td>2301</td> <td>A7</td> <td></td> </tr> </table>		PROGRAM ELEMENT NO.	PROJECT NO.	TASK NO.	WORK UNIT ACCESSION NO.	61102F	2301	A7	
PROGRAM ELEMENT NO.	PROJECT NO.	TASK NO.	WORK UNIT ACCESSION NO.									
61102F	2301	A7										
11. TITLE (Include Security Classification)												
(U) OPERATION AND UPGRADING OF THE BEAM OPTICS TEST STAND												
12. PERSONAL AUTHOR(S)												
Dr S. Humphries, Jr.												
13a. TYPE OF REPORT		13b. TIME COVERED		14. DATE OF REPORT (Year, Month, Day)								
Final		FROM 1 Nov 85 to 31 Mar 88		15. PAGE COUNT								
				84								
16. SUPPLEMENTARY NOTATION												
17. COSATI CODES			18. SUBJECT TERMS (Continue on reverse if necessary and identify by block number)									
FIELD	GROUP	SUB-GROUP										
	20-09		→ studied									
19. ABSTRACT (Continue on reverse if necessary and identify by block number)												
<p>This grant supported a two year study of novel methods to focus high intensity neutral particle beams. The work directly impacts the space based neutral particle beam program at Los Alamos National Laboratory. The goal was to investigate methods to correct aberrations in the final focusing lens of an NPB accelerator. The two unconventional beam optics techniques that were developed and investigated were 1) biased grid arrays to correct particle orbits and 2) solenoid lenses with entrapped non-neutral electron distributions to correct spherical aberration.</p>												
20. DISTRIBUTION / AVAILABILITY OF ABSTRACT			21. ABSTRACT SECURITY CLASSIFICATION									
X UNCLASSIFIED/UNLIMITED X SAME AS RPT. DTIC USERS			UNCLASSIFIED									
22a. NAME OF RESPONSIBLE INDIVIDUAL			22b. TELEPHONE (Include Area Code)									
B L SMITH			(202) 767-4908									
			22c. OFFICE SYMBOL									
			AFOSR/NP									

89 6 06 075

Final Report - Beam Optics Test Stand

FINAL REPORT

AIR FORCE OFFICE OF SCIENTIFIC RESEARCH
CONTRACT NO. AFOSR-86-0063

Operation and Upgrading of the Beam Optics Test Stand

-S. Humphries, Jr., Principal Investigator
Department of Electrical and Computer Engineering
University of New Mexico
Albuquerque, New Mexico 87131

This report completes a two-year study of novel methods to focus high-intensity neutral particle beams. The work directly impacts the space-based neutral particle beam program at Los Alamos National Laboratory. The goal was to investigate methods to correct aberrations in the final focusing lens of an NPB accelerator. The two unconventional beam optics techniques that we developed and investigated were 1) biased grid arrays to correct particle orbits and 2) solenoid lenses with entrapped non-neutral electron distributions to correct spherical aberration.

The report consists of three parts:

1. A reproduction of the paper "Correction of Charged Particle Beam Optics by a Programmed Electrostatic Wire Array," by S. Humphries, Jr. and R.L. Terry, published in the Journal of Applied Physics.

APOSR-TR- 89-0707

2. A reproduction of the paper "Experiments on a Space-charge-corrected Solenoid Lens," by S. Humphries, Jr. and R.L. Terry, submitted to the Journal of Applied Physics.
3. Photographs of the experimental apparatus constructed under the contract.



Accession For	
NTIS CRA&I	<input checked="checked" type="checkbox"/>
DTIC TAB	<input type="checkbox"/>
Unannounced	<input type="checkbox"/>
Justification	
By	
Distribution /	
Availability Codes	
Dist	Avail and/or Special
A-1	

SECTION 2

Correction of Charged Particle Beam Optics
by a Programmed Electrostatic Wire Array

-S. Humphries, Jr. and R.L. Terry
Institute for Accelerator and Plasma Beam Technology
University of New Mexico
Albuquerque, New Mexico 87131

ABSTRACT

Theoretical and experimental results are reported on a method for the correction of aberrations in optical elements for high power ion beams. The approach involves the use of arrays of wires immersed in large diameter beams. Individually controlled voltages are applied to the wires, resulting in local transverse deflections of beam particles. With regard to wire survivability and voltage requirements, the method appears feasible for application to high intensity negative ion beams. A formalism is described for the calculation of optimum wire voltages to achieve a specified beam angular correction in a Cartesian geometry. The results of the calculations were tested in modeling experiments using an 8 keV electron beam. The experimental array consisted of forty-six wires and boundary plates with independent applied voltages up to 3 kV. Voltage profiles for one-dimensional focusing, two-dimensional focusing, and beam steering were studied. The observed particle deflections and beam emittance growth due to the facet lens effect are in excellent agreement with predictions.

Correction of Charged Particle Beam Optics
by a Programmed Electrostatic Wire Array

-S. Humphries, Jr. and R.L. Terry
Institute for Accelerator and Plasma Beam Technology
University of New Mexico
Albuquerque, New Mexico 87131

1. Introduction

Theoretical and experimental results are reported on the correction of charged particle optical elements using arrays of wires with individually controlled bias voltages. The wire arrays can create local components of transverse electric fields to cancel errors in lenses and beam steering elements and to compensate deflections arising from non-linear space charge forces. There is a substantial body of past research on grid lenses for electron beam optics [1,2,3,4]. These lenses utilize unipotential planar or shaped meshes that traverse the beam. The meshes act in concert with external electrodes to focus the beam or to correct spherical aberration in a conventional lens. In the past, wire arrays with spatial variations of applied voltage have not been utilized in small systems because of the complexity of fabrication and operation. With modern methods of computer control for complex systems, biased wire arrays with multiple voltage levels may be feasible for optical correction in high energy accelerators.

In this paper, the theory of wire arrays with a Cartesian geometry is derived. The theory predicts optimum wire voltages to correct known spatially dependent angular errors in charged

particle lenses and deflectors. The results of experiments to test the validity of the theory are reported. The modeling experiments used a low current 10 keV electron beam passing through an array of 42 individually controlled wires.

Our work was motivated by the possible use of neutral hydrogen beams for space based defense applications [5]. The Neutral Particle Beam concept involves the creation of an atomic beam from an energetic beam of H^- ions. The atomic beam must have excellent directionality to converge to a target following ballistic orbits over long distances. In order to meet this condition, the negative ion beam must have very low emittance and the output optical elements of the accelerator must have high accuracy. For a given beam emittance, the spot size at the target is minimized by making the diameter of the output focusing lens as large as possible. Unfortunately, limitations set by lens aberrations increase with lens diameter. The correction of aberrations using conventional techniques involves complex optical systems [6] with size and mass far beyond those tolerable for mobile systems.

Space-based accelerators will also set strong requirements on steering elements. The spatial force variations of large aperture beam deflectors would enhance the spread in transverse angle unless compensated. It may be necessary to sweep deflection fields on a rapid time scale; any method of compensation must be able to track these variations. The optical correction system should have low mass and fast response. The ideal system would be

interactive, responding to beam diagnostics on the space platform and return signals from the target. Biased wire arrays have a number of favorable characteristics for the application. The associated hardware is robust and is light. Wire voltages can be varied on submicrosecond time scales. The major feasibility issue for the application of wire arrays is whether appropriate correction profiles can be achieved within the limits of practical construction.

This paper addresses some aspects of the use of electrostatic grids in large diameter optical elements for high average power ion beams. Feasibility issues, such as wire survivability and voltage requirements, are discussed in Section 2. Section 3 outlines the theory of beam deflection by the Cartesian wire array used in the experiments. The electron beam experimental apparatus is described in Section 4. Experimental results are summarized in Section 5

2. Feasibility issues for biased wire arrays in high average power ion beams

A basic requirement for the applications of biased arrays to ion beam focusing is that the wires in a high transparency matrix can survive bombardment by the beam. It is essential that the temperature of the wires does not approach the melting point. Consider a wire of diameter δ immersed in an ion beam with kinetic energy E_i , total current I , and diameter r_b . The power deposited in the wire per unit length is approximately

$$P_{in} \text{ (watts/m)} = (I/e\pi r_b^2) (dE_i/dx) \delta^2, \quad (1)$$

where dE_i/dx is the ion stopping power. Assuming that the wires at temperature T are in a radiation equilibrium with low temperature surrounding walls at temperature T_w , the power radiated per length of wire is approximately

$$P_{out} \text{ (watts/m)} = (\pi\delta) \sigma(T^4 - T_w^4) \cong (\pi\delta) \sigma T^4, \quad (2)$$

where σ is the Stefan-Boltzmann constant. Setting the powers of Eqs. 1 and 2 equal gives the following expression for the wire temperature:

$$T = \left[\frac{I (dE_i/dx) \delta}{e \pi^2 r_b^2 \sigma} \right]^{1/4}. \quad (3)$$

As an example, consider a 200 MeV H^- beam with a current of 0.5 A; the wires are situated in a large diameter lens for final beam focusing. The beam radius is taken as $r_b = 0.15$ m and the wires are composed of tungsten with a 1 mil ($\delta = 2.5 \times 10^{-5}$ m) diameter. The stopping power for 200 MeV H^- ions in tungsten [7] is about 9×10^{-10} J/m. Inserting the parameters into Eq. 3 gives an equilibrium temperature of only 1200 °C, well below the melting point of 3410 °C. Wires exposed to a high power ion beam will be strongly heated but should not be immediately destroyed. Problems associated with non-uniform thermal expansion can be avoided if the wires are stretched in straight lines across beam volume with a spring mount.

A second issue is whether significant focusing effects can be achieved with reasonable voltages. Again, we consider focusing 200 MeV H^- ions in the final lens of a large diameter beam telescope. The final lens has a 10 m focal length; the maximum beam radius is $r_b = 0.15$ m. A reasonable requirement for a correction system is a 1 per cent modification of the maximum angle of deflection in the lens [8]. For the parameters given, the maximum correction angle is $\Delta\theta = 0.3$ mrad. The required magnitude of a transverse electric field acting over a length ℓ is:

$$E_{\perp} \cong 2(T_i/e)\Delta\theta/\ell, \quad (4)$$

where T_i is the ion kinetic energy. For $\ell = 0.3$ m, the transverse field equals $E_{\perp} = 0.4$ MV/m, a moderate value. The voltage to produce such a field is in the range of 100 kV. The relatively high voltage value can be reduced by extending the interaction length of the wire array; this approach has the disadvantage of reduced structural transparency.

In addition to the macroscopic fields generated by the wire arrays, there are local electric field perturbations around individual elements. This effect, known as *facet lens focusing*, is a problem whenever grids are used in charged particle optic systems [9]. The electric fields around a one-dimensional array of wires in the presence of an applied axial field are illustrated in Fig. 1. The local fields act to focus or defocus particles about the midplane between wires. The approximate focal length for facet lens focusing [10] for a one-dimensional array of wires

separated by distance d is

$$f \cong 2T_i/q(E_{z2} - E_{z1}). \quad (5)$$

In Eq. 5, T_i is the kinetic energy of particles with charge q , E_{z1} is the average axial electric field on the upstream side of the wire array, and E_{z2} is the field on the downstream side.

The facet lens effect results in deflection of beam particles on a scale size comparable to the array spacing. This modifies the beam distribution leading to emittance growth [11]; the perturbed distribution is indicated as a dashed line in Fig. 2a . The intended function of the wire array is to apply macroscopic forces with programmed spatial variations to correct angular errors in the distribution; the corrected distribution is illustrated in Fig. 2b. Inspection of the figure shows that the presence of wire arrays will improve the quality of a beam emerging from an imperfect lens if the angular errors from facet lens focusing are small compared to the net correction angle. The relative effect of facet lens focusing can be estimated in the geometry illustrated in Fig. 3. Assume there are two ground planes composed of fine meshes on each side of a linear wire array with spacing d and distance D from the ground plane. At the point of interest, there is a voltage V applied to the wire array. From Eq. 5, the maximum facet lens deflection of a particle passing through the array is

$$\Delta\theta_f = (d/2)/f = (eV/2T_i) (d/D). \quad (6)$$

The highest value of macroscopic transverse field that can be

achieved with the wires is about $E_{\perp} \sim (V/2D)$. Substitution in Eq. 4 implies an ordered beam deflection of

$$\Delta\theta = D(V/2D)/(2T_i/e) = (eV/2T_i) \quad (7)$$

The ratio of the random deflection angle to the ordered angle is about $\Delta\theta_f/\Delta\theta \cong (d/D)$. Inspection of Eq. 7 shows that the presence of the wire array leads to a net improvement in the beam quality if the spacing between wires is small compared to the distance over which the transverse fields act, $d \ll D$.

3. Theory of the Cartesian array in the paraxial limit

The constraints of practical construction place limitations on the forms of angular deflections of charged particles that can be achieved by wire arrays. The two major problems are 1) mechanical supports, and 2) voltage leads. With regard to the first point, it is unlikely that thin wires can be formed into rigid curves that will accurately preserve their shape under the thermal and mechanical stress of applications. Limitations of material properties dictate that the wires of an array must follow straight lines. In this case, the wires can be spring mounted so that they do not sag when heated or break when subjected to vibration. The wire support structures and bias voltage connections must be located outside the beam volume. Bare or insulated wires crossing the beam volume would lead to severe distortions of the applied electric field.

Within the constraint of external connections, there is a

variety of geometries that can, in principle, provide different forms of angular correction. In this paper, we shall concentrate on the simple geometry illustrated in Fig. 4. A set of biased wires parallel to the y-axis is located between two ground planes. The axial distance to the ground planes on both side of the wire array is denoted d . The wire voltages can be adjusted individually. The wires are assumed to extend an infinite distance in the y-direction. In order to apply a Fourier series analysis, the profile of voltages on the wires is assumed to repeat periodically in the x-direction over an interval $2D$. The analysis approximates the fields from a single set of wires if the distance D is chosen large compared to the beam halfwidth and to the axial spacing between electrodes, $D \gg d$. By symmetry, bias voltages on the wires can generate only components of electric field in the x-direction. In consequence, the wire array illustrated can impose an angular correction of the form $\Delta\theta_x(x)$ on a charged particle beam moving through the system in the z-direction.

The problem of optical correction of a charged particle beam can be expressed in the following manner. Given a known beam aiming error function, $-\Delta\theta_x(x)$, the goal is to find a set of wire voltages that produces a deflection $\Delta\theta_x(x)$. It is assumed that there are many wires so that the electrostatic potential in the plane $z = 0$ can be approximated by a continuous function $\phi(x, 0)$. This assumption is equivalent to the neglect of facet lens effects. To facilitate the mathematical analysis, the aiming error is taken as a periodic function of x . It is clear that a

requirement for a valid solution is that $\Delta\theta_x(x)$ varies continuously over scale lengths comparable to or longer than d .

The Laplace equation in the region between the wire array and ground plane can be solved by the method of separation of variables [12]. Assume the potential can be expressed in the form

$$\phi(x, z) = \phi(x)\phi(z). \quad (8)$$

The solution will be performed in the region in the region $0 \leq z \leq d$. By symmetry, there is a mirror field pattern in the region $-d \leq z \leq 0$; the additional fields double the total deflection of particles in the x -direction. An electrostatic potential of the form of Eq. 8 can be expressed in terms of series expansion of orthogonal functions. The Cartesian geometry of the system and the assumed periodicity in the x -direction gives the following form:

$$\phi(x, z) = \phi_0 + \sum_{n=1}^{\infty} \left[A_n \cos \left(\frac{n\pi x}{D} \right) + B_n \sin \left(\frac{n\pi x}{D} \right) \right] f_n(z). \quad (9)$$

The even terms (with coefficients A_n) correspond to electrical forces that are symmetric about the system axis and plane $x = 0$. Symmetric forces focus (or defocus) charged particles traversing the system. The odd terms (with coefficients B_n) correspond to steering forces.

Eq. 9 is a valid electrostatic potential if there is a

function, $f_n(z)$, that satisfies the Laplace equation and the boundary conditions in the region of interest. The axial function obeys the following equation:

$$\frac{\partial^2 f_n}{\partial x^2} - \left[\frac{n\pi}{D} \right]^2 f_n = 0. \quad (10)$$

The solution of Eq. 10 with the boundary condition $\phi(0,d) = 0$ is:

$$f_n(z) = \frac{\exp(-\alpha_n z) - \exp(-2\alpha_n d)\exp(\alpha_n z)}{(1 - \exp(-2\alpha_n d))}. \quad (11)$$

where $\alpha_n = (n\pi/D)$.

The quantity of interest for calculating particle deflections is the transverse electric field, $E_x = -\partial\phi/\partial x$. Substitution from Eqs. 9 and 10 gives the following expression:

$$E_x = \sum_{n=1}^{\infty} \alpha_n [A_n \sin(\alpha_n x) - B_n \cos(\alpha_n x)] \times \left[\frac{\exp(-\alpha_n z) - \exp(-2\alpha_n d)\exp(\alpha_n z)}{(1 - \exp(-2\alpha_n d))} \right]. \quad (12)$$

In the paraxial limit, the transverse motion of a non-relativistic particle is determined by:

$$\frac{dv_x}{dz} \approx \frac{eE_x}{m_0 v_z} . \quad (13)$$

The paraxial limit is defined by the condition that the transverse velocity of a particle is small compared to the axial velocity, $v_x \ll v_z$. This condition implies that the axial velocity is almost constant and that the lateral translation of a particle crossing the region between $z = 0$ and $z = d$ is small compared to d .

Integration of Eq. 13 shows that the net angular deflection of a particle of mass m_0 and charge Ze induced by the grid wire voltages is given by

$$\Delta\theta_x(x) = \frac{\Delta v_x}{v_z} = 2 \frac{Ze}{m_0 v_z^2} \int_0^d E_x(x, z) dz = \frac{2e\langle E_x(x) \rangle}{m_0 v_z^2} . \quad (14)$$

The factor of 2 represents the cumulative effect of regions on both sides of the wires. The average electric field in Eq. 14 can be expressed in terms of the coefficients of the series expansion for potential by carrying out the axial integral over Eq. 12:

$$\langle E(x) \rangle = \sum_{n=1}^{\infty} [A_n \sin(\alpha_n x) - B_n \cos(\alpha_n x)] \left[\frac{\{1 - \exp(-\alpha_n d)\}^2}{d \{1 - \exp(-2\alpha_n d)\}} \right] \quad (15)$$

The angular error appearing in Eq. 14, $\Delta\theta_x(x)$, is a given periodic function of x . The function can be expressed as a Fourier series:

$$\theta_x(x) = \sum_{n=1}^{\infty} \left[\theta_{en} \cos\left(\frac{n\pi x}{D}\right) + \theta_{on} \sin\left(\frac{n\pi x}{D}\right) \right] \quad (16)$$

where the coefficient θ_{en} and θ_{on} are evaluated by standard methods. Comparison of Eqs. 14 and 16 leads to the following expressions for the coefficients of the potential expansion:

$$B_n = - \left[\frac{\theta_{en} d m_o v_z^2}{2Ze} \right] \left\{ \frac{1 - \exp(-2\alpha_n d)}{[1 - \exp(-\alpha_n d)]^2} \right\} \quad (17)$$

and

$$A_n = \left[\frac{\theta_{on} d m_o v_z^2}{2Ze} \right] \left\{ \frac{1 - \exp(-2\alpha_n d)}{[1 - \exp(-\alpha_n d)]^2} \right\} \quad (18)$$

Once the potential coefficients are known, the optimum wire voltages can be determined by evaluating ϕ at $z = 0$;

$$\phi(x,0) = \phi_0 + \sum_{n=1}^{\infty} \left[A_n \cos \left(\frac{n\pi x}{D} \right) + B_n \sin \left(\frac{n\pi x}{D} \right) \right] \quad (19)$$

A computer program was written to carry out the mathematical operations of Eqs. 16 through 19. Input to the program was an angular deflection function; the output was a set of wire voltages to compensate the deflection. The program also computed settings for the resistive ladder network used in the experiments to supply voltage to the 42 wire array. An example of the calculation of wire settings to achieve a line focus for the parameters used in the modeling experiment is illustrated in Fig. 5. The beam kinetic energy was 8 keV and the distance between the wire array and ground plane was $d = 0.0254$ m. The periodic angular function used as input is shown in Fig. 5a. The function corresponds to a linear focus over the region $-0.75D < x < 0.75D$, where $D = 0.15$ cm. The linear function extending to ± 0.113 cm provides a good overlap of the 0.03 m halfwidth beam. The assumed function drops to zero at D to facilitate convergence of the Fourier terms. The angle $\Delta\theta_0$ is defined as the magnitude of the deflection at $D/2$, corresponding to the outer edge of the beam. For the example, $\Delta\theta_0$ equals 0.2, corresponding to a focal length for the array of 0.375 m. The voltage profile over the beam width calculated using 25 terms in the Fourier analysis is plotted in Fig. 5b. The wire voltages used to achieve a finite element approximation of the profile are also indicated.

The Cartesian wire array has the interesting property that two sets of wires can be combined in the same device to provide independently controlled deflections in the x and y directions. In the experiments, two sets of biased wires were enclosed between ground planes. The wires of one set were parallel to the y-direction (Y wires), while the other set was oriented along the x-direction (X-wires). Voltages on the Y wires created electric fields with only an x-component. Electric fields in the x-direction were shorted out in the plane of the X wires. Therefore, the X wires acted as a ground plane for the transverse electric fields created by the Y wires. Conversely, the Y wires acted as a ground plane for the E_y field from the X wires. The result was that the voltages on the Y wires and X wires acted independently to deflect particles in the x and y directions respectively.

4. Experimental apparatus

Experiments were carried out using an array of 42 individually biased wires to focus and to steer an 8 keV, 100 μ A electron beam. The experimental apparatus is illustrated in Fig. 6. The assembly to generate the beam [8] was based on a commercial 3 keV electron gun with oxide cathode and a post-acceleration gap of our own design. An einzel lens in the gun was used to control the beam diameter at the wire array. The beam was aimed by a magnetic deflector with nested cosine coils. The distance from the gun to the wire array was 0.78 m; the intervening vacuum chamber was shielded with μ -metal. Adjustment of the beam position and

current was performed with a phosphor coated current collector on a movable vacuum extension.

After passing through the array, the beam entered a drift tube of length 0.83 m. The drift tube was not magnetically shielded so a bias field was applied along its length to cancel the effect of the Earth's magnetic field. A 7.9 cm wide phosphor was located at the end of the tube to measure the transverse beam profile. The phosphor was mounted on a glass plate for observations in the forward direction. The phosphor was coated with a thin but opaque layer of graphite to relieve charge accumulation. of graphite. The beam profile was recorded by time-integrated photographs.

A detailed view of the wire array assembly is shown in Fig. 7. The 42 wires were supported inside an acrylic cylinder by 84 vacuum feedthroughs. The 0.005 cm diameter stainless steel wires were spaced a uniform transverse distance 0.51 cm apart. The tension in each wire was maintained with a miniature compression spring. Lateral boundary conditions for each wire set were determined by two end plates. Independent voltage could be applied to all the wires and the four plates by connections external to the vacuum. The wire sets were spaced an axial distance 2.54 cm apart. A geometry equivalent to the theoretical model of Section 3 was achieved by locating ground planes 2.54 cm upstream and downstream from the wire arrays. The ground plane consisted of a highly transparent stainless steel mesh composed of 0.0025 cm diameter wires.

The multiple voltages were supplied by two series networks of

floating potentiometers. The divider circuit could sustain a voltage drop of 3 kV. Potential levels were adjusted with a digital voltmeter at low bias. The divider network was biased to a peak voltage in the range 0-3 kV. The effect of a particular voltage profile could be varied by adjusting the supply voltage.

5. Experimental results

Initial tests were carried out to observe facet lens distortion of the beam passing through the wire array. All the X-wires were connected in parallel and biased to the same voltage; therefore, there were no large scale focusing or steering forces in the y-direction. The Y-wires were also connected in parallel. Separate voltages could be applied to the X and Y-wires. The beam was expanded to a 4 cm diameter at the position of the wire array.

A photographic image of the beam profile at the end of the drift tube is shown in Fig. a for a case where the X wires were grounded and a negative voltage was applied to the Y wires. An applied voltage of -250 V gave the best line pattern for a 4.0 keV beam. Note that the deflections were purely in the x-direction. As expected, a negative wire voltage resulted in a facet lens effect with a positive focal length. Electrons passing between two wires were focused to the midplane between wires. The distance between line foci in Fig. 8a was about twice the spacing between wires, as expected from the geometry of the system (Fig. 7b). A positive array voltage caused defocusing of electrons

about the midplane between wires. Fig. 8b represents a case with a positive voltage (+450 V) applied to the X wires with the Y wires grounded. As expected, slices of the beam were defocused. The line pattern observed at high voltage was caused by overlap of defocused electrons from adjacent slices.

Fig. 9 shows the profile of an 8 keV beam when equal negative voltages of -820 V were applied to both wire sets simultaneously. Note that focusing in the x-direction was unaffected by the non-zero potential of the Y wire array. Focusing in both directions was almost identical, resulting in a pattern of point foci oriented at an angle of $\pm 45^\circ$ with respect to the wires. The results observed were in good quantitative agreement with predictions from Eq. 6. Since both sets of wires had the same potential, there was no axial electric field between the sets. In consequence, the change in electric field appearing in Eq. 6 was only $\Delta E_z = V_0/d = 820/2.54 \times 10^{-2} \text{ V/m} = 32.3 \text{ kV/m}$ for the focal length in each direction. The expected facet lens focal length is $f = 2T_e/\Delta E_z = 39.6 \text{ cm}$. The experimental data can be analyzed with the thin lens formula:

$$f = \left[\frac{1}{d_1} + \frac{1}{d_2} \right]^{-1} \quad (20)$$

In Eq. 20, f is the facet lens focal length corresponding to an optimum line focus, d_1 is the distance from the gun output to the wire array and d_2 is the distance from the wires to the detector. Inserting the geometric parameters of the system, Eq. 20 predicts

a focal length of 40.2 cm, in good agreement with the facet lens prediction.

Initially, focusing experiments were carried out with independent voltages on both the X and Y-wires. Because of limitations on the potentiometers, the wire voltages and beam energy were relatively low. Optimum relative voltages were calculated using the method discussed in Section 3. After the relative voltage profile was set, the magnitude of the voltage was adjusted for the best focus. The theory constrains only the voltage differences between wires; the choice of absolute potential of the array relative to the ground planes is arbitrary. In the initial experiments, the wire voltages were negative. The voltage on axis was zero, while the maximum amplitude was applied at the endplates. Although the choice of absolute potential had little effect on focal properties of the wire array, the absolute potential determined the magnitude of axial electric fields and facet lens deflections. With the wire potential equal to zero at the array center, axial electric fields were small in the region occupied by most of the particles of the 4 cm diameter beam. In consequence, the particular choice of absolute potential minimized facet lens distortion of the beam distribution.

Results on beam focusing were in good agreement with predictions. Photographs of focused beam profiles are shown in Fig. 10. The X and Y-Wire circuits were driven by separate power supplies. Initially, the X-wire voltage input was clamped to 0 V while the Y-wire maximum voltage was adjusted for the best line

focus. Fig. 10a shows the beam profile obtained with a peak Y-wire voltage input -540 V. This value was quite close to the theoretical prediction of -510 V. Similar results were obtained with the Y-Wires grounded and -540 V applied to the X-Wires (Fig. 10b. Finally, Fig. 10c shows the results of applying -540 V to both sets of wires simultaneously. As expected, the focusing properties of both wire sets acted independently. A plot of the beam intensity measured from the photograph is shown in Fig. 10d. The focused beam profile has a full width at half-maximum of 0.75 cm. The focal properties of the beam emerging from the wire array infers an emittance of $7.2 \times 10^{-5} \pi \text{ m rad}$, compared to an inherent electron gun of $1.6 \times 10^{-5} \pi \text{ m rad}$.

Focusing experiments were conducted at high beam kinetic energy (8 keV) using a modified potentiometer array that could control voltages as high as 3 kV. Both sets of wires were driven in parallel for a two-dimensional focus. Applied voltages were positive. Although the voltage shape function was the same as in the low energy experiments, the maximum potential was applied to the central wires while the endplates were held at ground potential. Even though large scale focusing forces were the same as the previous experiments, the emittance dilution caused by facet lens effects was much more severe. A photograph of a beam profile under these conditions for wire voltages adjusted for the best focus is shown in Fig. 11. The overlapping particle orbits filled a large square area. The full width at half-maximum of the focal spot varied weakly with voltage around the optimum because of the dominance of emittance. The minimum observed width was 3.3

at a peak voltage of about -2000 V, within 5% of the prediction of model of Section 3. The width of the beam was well described by Eq. 6. The predicted peak facet lens deflection angle for on-axis particles at 2000 V was 15 mrad, implying that the width of the focal spot should have exceeded 2.5 cm. The size of the focal spot was dominated by facet lens distortion at the center of the wire array. As expected, the size of the focal spot was relatively independent of the size of the beam at the wire array. The spot diameter changed less than 10% for a variation of beam diameter at the lens of 1 to 4 cm.

Experiments were also performed using the electrostatic arrays to steer the beam. A bipolar voltage profile predicted from the model of Section 3 was applied to the Y-wires. The profile had zero voltage at the center to minimize emittance growth of the beam. The lens of the electron gun was adjusted to produce a minimum spot size at the detector phosphor. Fig. 12 shows photographic data of beam deflection for three values of the peak wire voltage. The photographs are double exposures showing the beam position with and without application of the wire voltage. The measured deflections scale linearly with wire voltage. They are within 5% of absolute predictions from the theory of Section 3.

The utilization of biased wires for optical correction of negative ion beams was suggested to us by John Browning of the Air Force Weapons Laboratory. We would like to thank D. Straw, T. King and J. McHarg for their interest in the work, and G. Hess,

J. Farrel and K. Halbach for their technical suggestions. This work was supported by the Air Force Office of Scientific Research under Contract No. AFOSR-86-0063.

REFERENCES

1. See, for instance, P. Grivet, *Electron Optics, Part 1*, translated by P.W. Hawkes (Pergamon Press, Oxford, 1972), Section 8.3.
2. M.Y. Bernard, C.R. Acad. Sci. Paris 233, 289 (1951) and J. Physics Radium 14, 451 (1953).
3. O.I. Seman, Zh. Tekh. Fiz. 22, 1581 (1952).
4. See, for instance, K.L. Hanszen and R. Lauer, "Electrostatic Lenses" in *Focusing of Charged Particles, Vol. 1*, edited by A. Septier (Academic Press, New York, 1967), 271.
5. R.A. Jameson, Nucl. Instrum. and Methods B24/25, 725 (1987).
6. See, for instance, R.V. Servranckx and K.L. Brown, Nucl. Instrum. and Methods A258, 525 (1987).
7. See, for instance, G.F. Knoll, *Radiation Detection and Measurement* (John Wiley and Sons, New York, 1979), 53.
8. G. Hess and S. Humphries, Jr., J. Appl. Phys. 60, 1571 (1986) and Nucl. Instrum. and Methods A258, 572 (1987).
9. P. Grivet, *op.cit.*, 89.

10. See, for instance, S. Humphries, Jr., *Principles of Charged Particle Acceleration* (John Wiley and Sons, New York, 1986), 121.
11. F. Bertein, *J. Phys. Radium* 12, 595 (1951).
12. See, for instance, J.D. Jackson, *Classical Electrodynamics* (John Wiley and Sons, New York, 1962), 47.

FIGURE CAPTIONS

1. Origin of facet lens focusing - distortion of electric fields in the vicinity of grid wires.
2. Effects of electric fields from a biased wire array on a beam trace space distribution. a) Local angular distortion from the facet lens effect resulting in emittance growth. b) Desired macroscopic angular correction and emittance reduction for a beam distribution distorted by lens aberrations.
3. Geometry for estimation of relative angular deflection from macroscopic electric fields and wire perturbation fields.
4. Cartesian wire array geometry for programmed particle deflections in x-direction.
5. Predicted voltage profile for a one-dimensional beam focus. a) Desired angular deflection function for a line focus. Parameters for experiment: $D = 0.152$ m, $\theta_0 = 0.20$ rad. b) Predicted voltage profile and levels for a twenty-three wire array. Parameters for an axial spacing from the wires to ground planes of $d = 0.0254$ m and an 8 keV beam energy.

6. Experimental apparatus, electron beam modeling experiment.
7. Scale drawings of wire array assembly. a) Side view. b) End view.
8. Facet lens effects. 4 keV beam, 0.83 m from array to detector
a) X-wires grounded, 4 keV beam, -250 V applied to Y-wires. b) Y-wires grounded, +450V applied to X-wires polarity.
9. Dual directional facet lens focusing, 8 keV beam, -820 V applied to both X and Y-wires.
10. Focusing results, 2 keV beam. a) -540 V peak on Y wires. b) -540 V peak on X wires. c) Focusing in both directions.
11. Focusing voltage profile, bidirectional. Maximum voltage at center of array. 8 keV beam. +2000 V peak on X and Y-wires.
12. Beam deflection, scaling with peak deflection voltage. X-wires grounded, deflection profile on Y-wires. 4 keV beam. Double exposure, with and without Y-wire voltage. Peak voltage: a) 500 V, b) 600 V, c) 700 V.

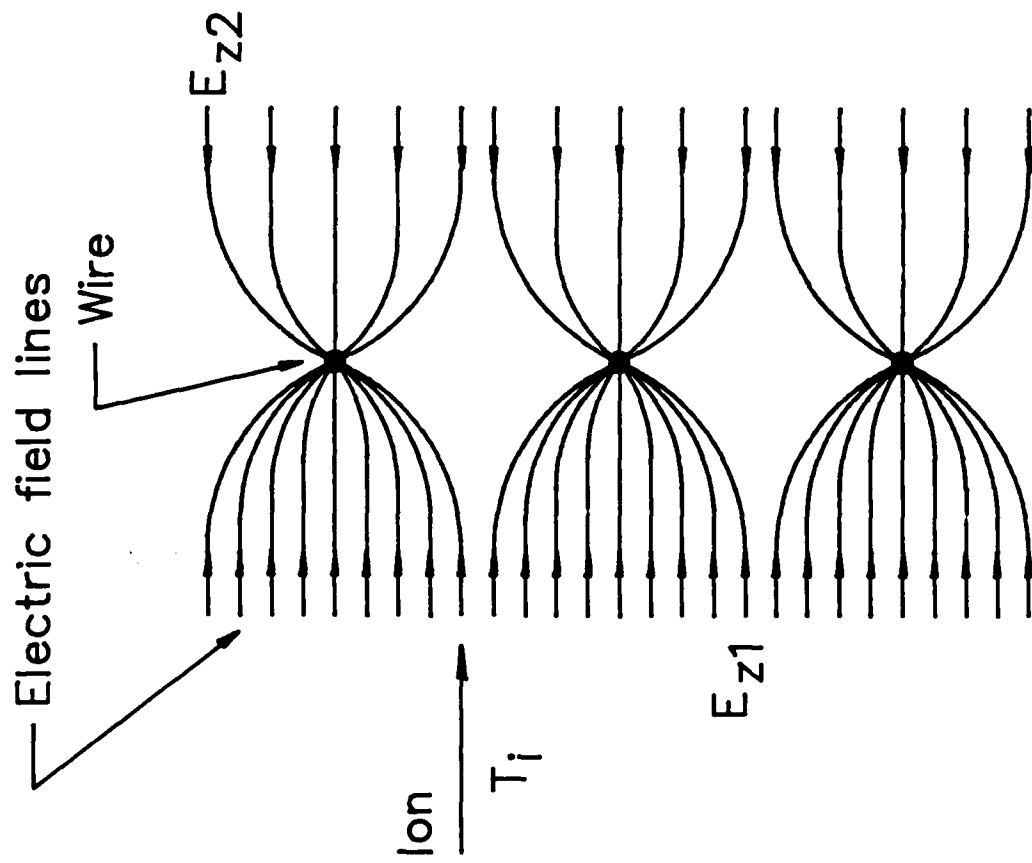
SECTION 3

Experiments on a Space-charge-corrected Solenoid Lens

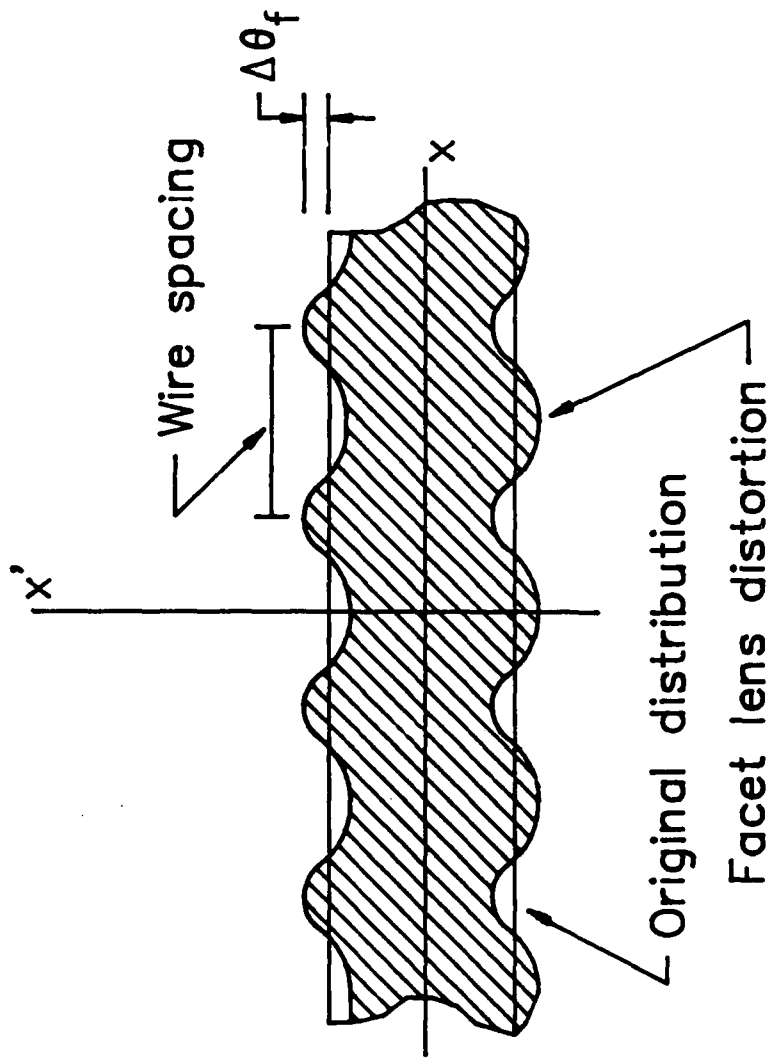
-Stanley Humphries, Jr. and R.L. Terry
Department of Electrical and Computer Engineering
University of New Mexico
Albuquerque, New Mexico 87131

ABSTRACT

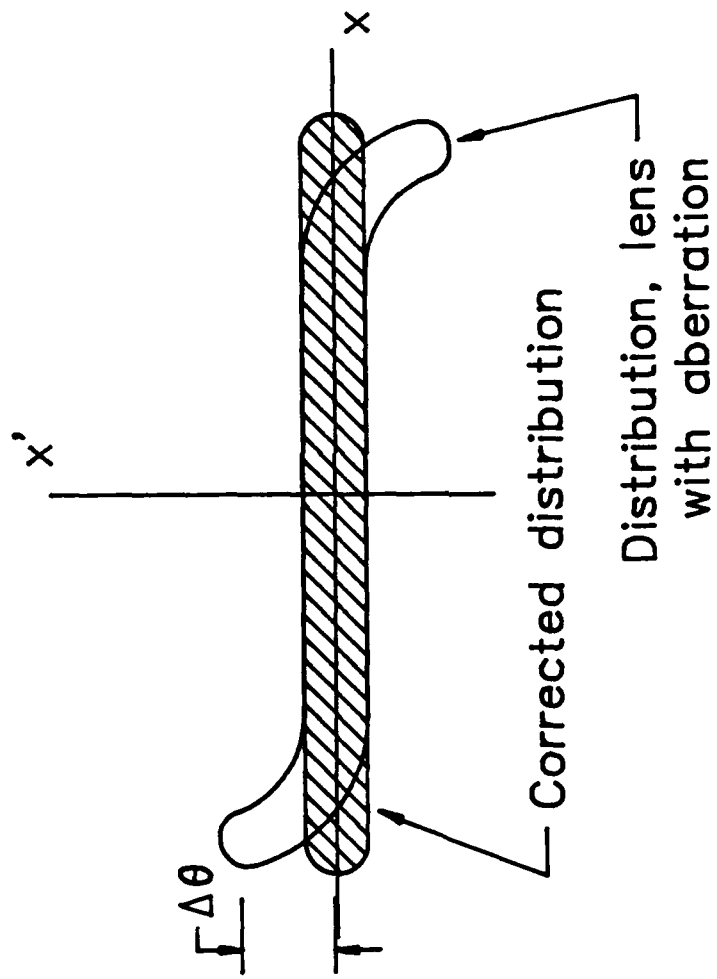
We describe experiments on trapped, non-neutral electron distributions for the correction of spherical aberration in solenoidal lenses. The method is best suited to beams of negative ions - our work was motivated by potential applications to space-based neutral-particle-beam accelerators. The experiments demonstrate that it is possible to control the space-charge potential of the electrons through bias voltage settings on external electrodes. We observed radial electric fields of 40 kV/m - this figure is within the range of interest for the application. We created annular electron distributions with fluctuating fields less than one per cent of the steady-state value. We attribute suppression of the diocotron instability to electron conduction along magnetic field lines. Although the fluctuations were small, the level was still an order of magnitude higher than requirements for the final focusing lens of space-based accelerators.

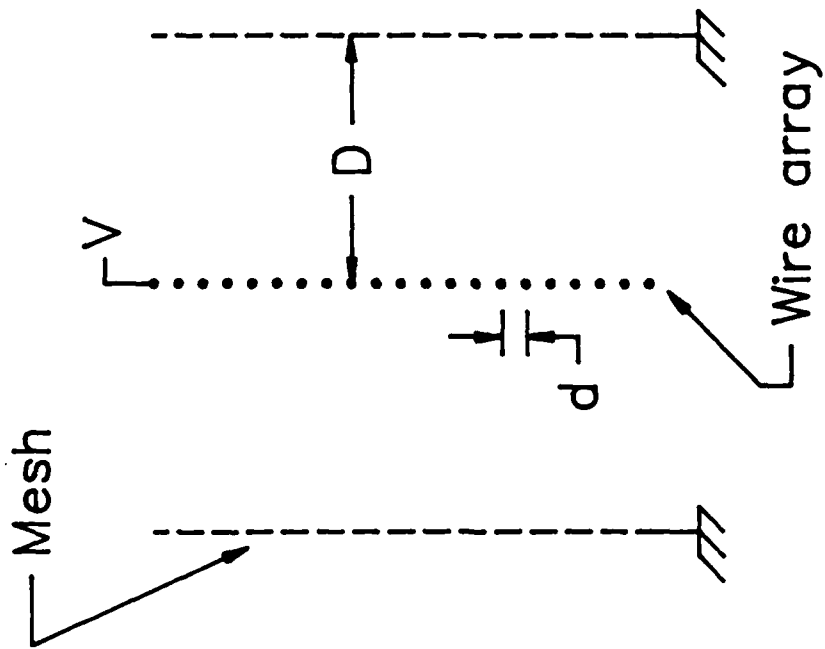


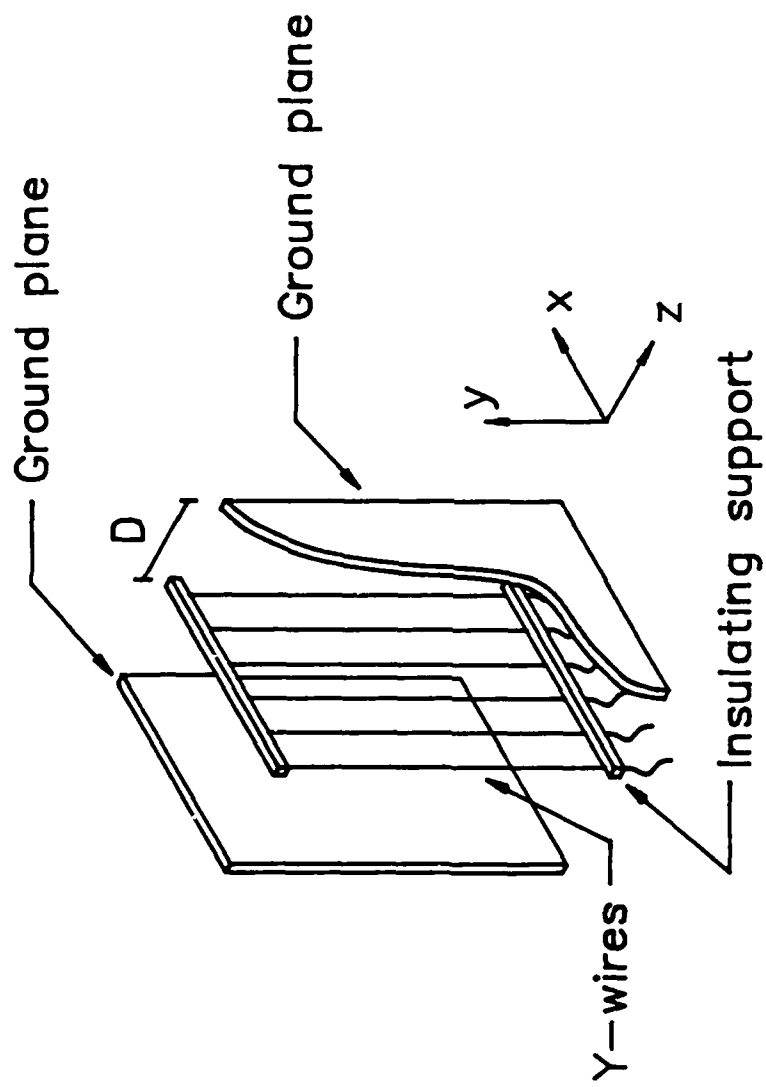
a)



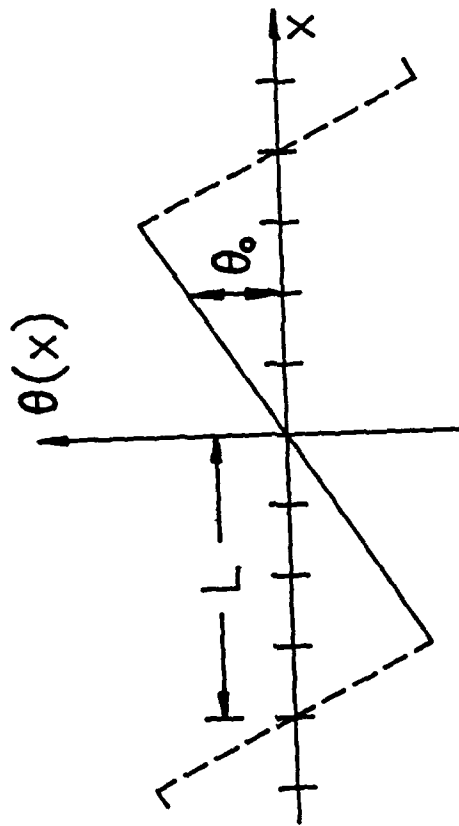
b)



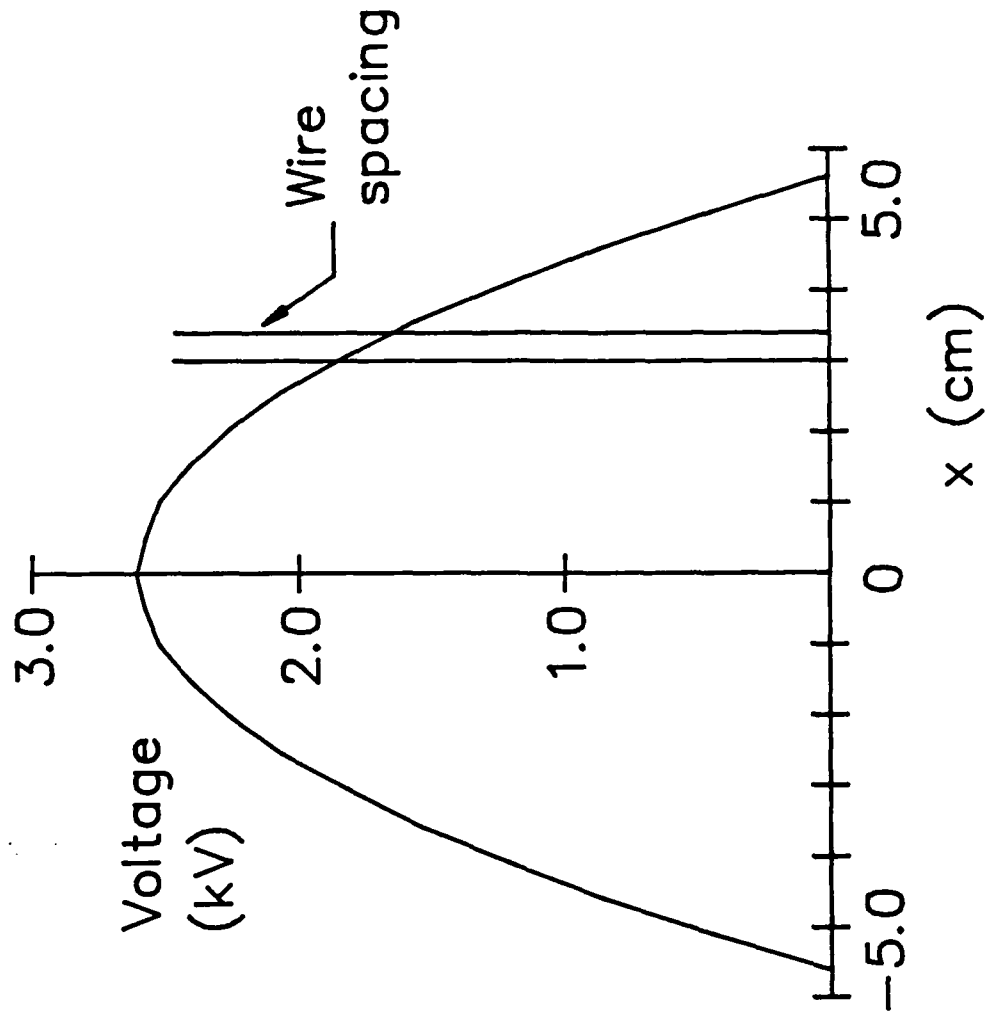


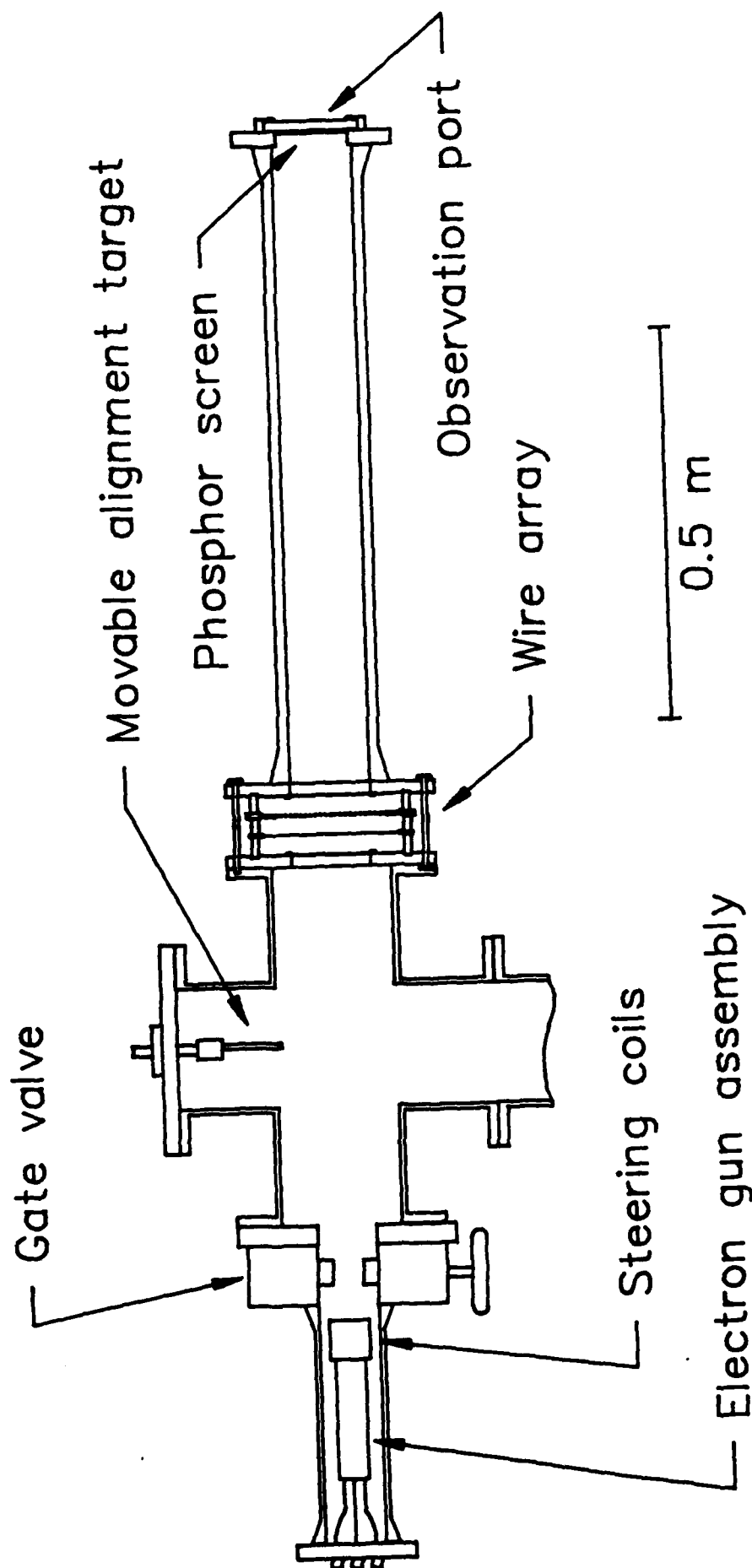


a)

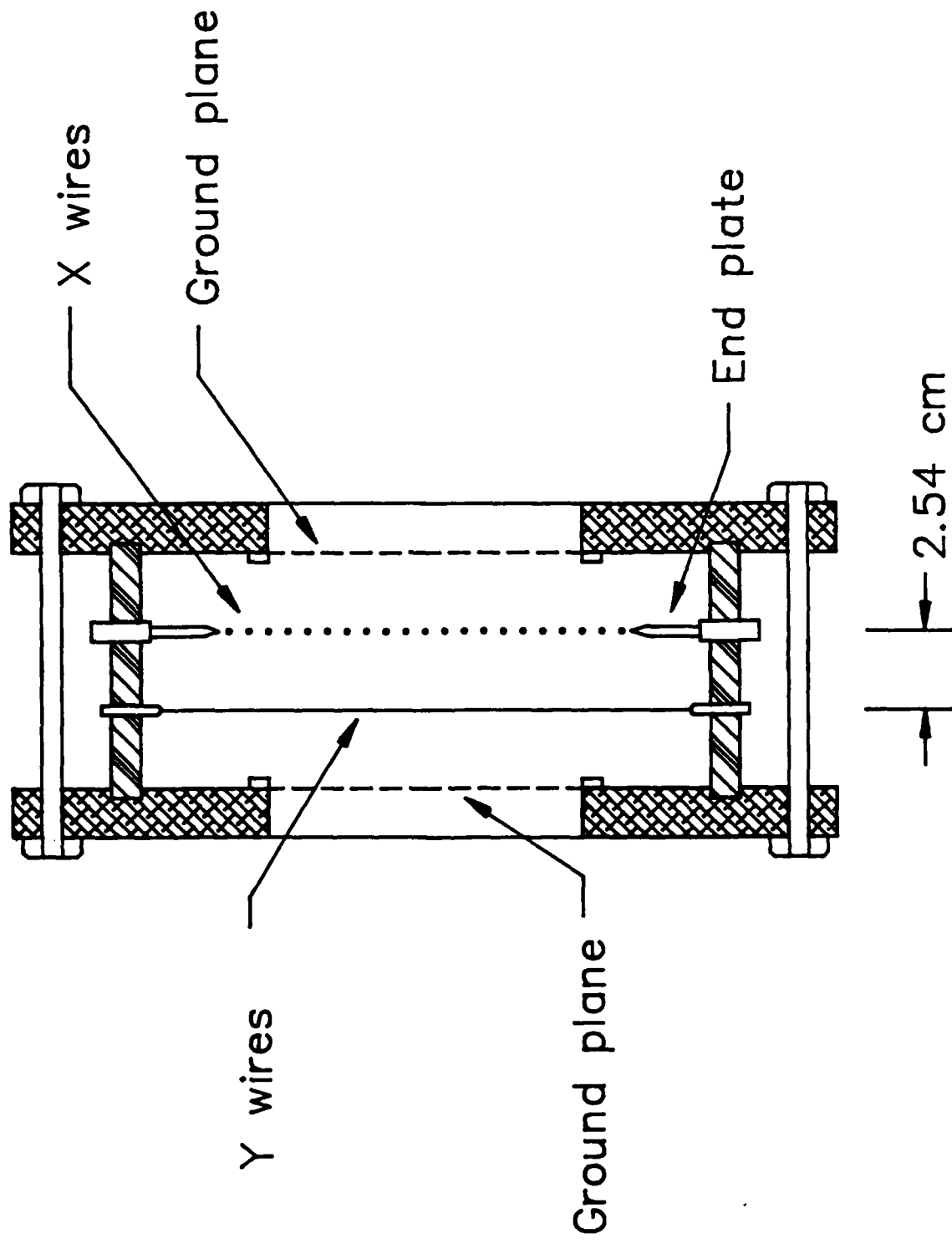


b)

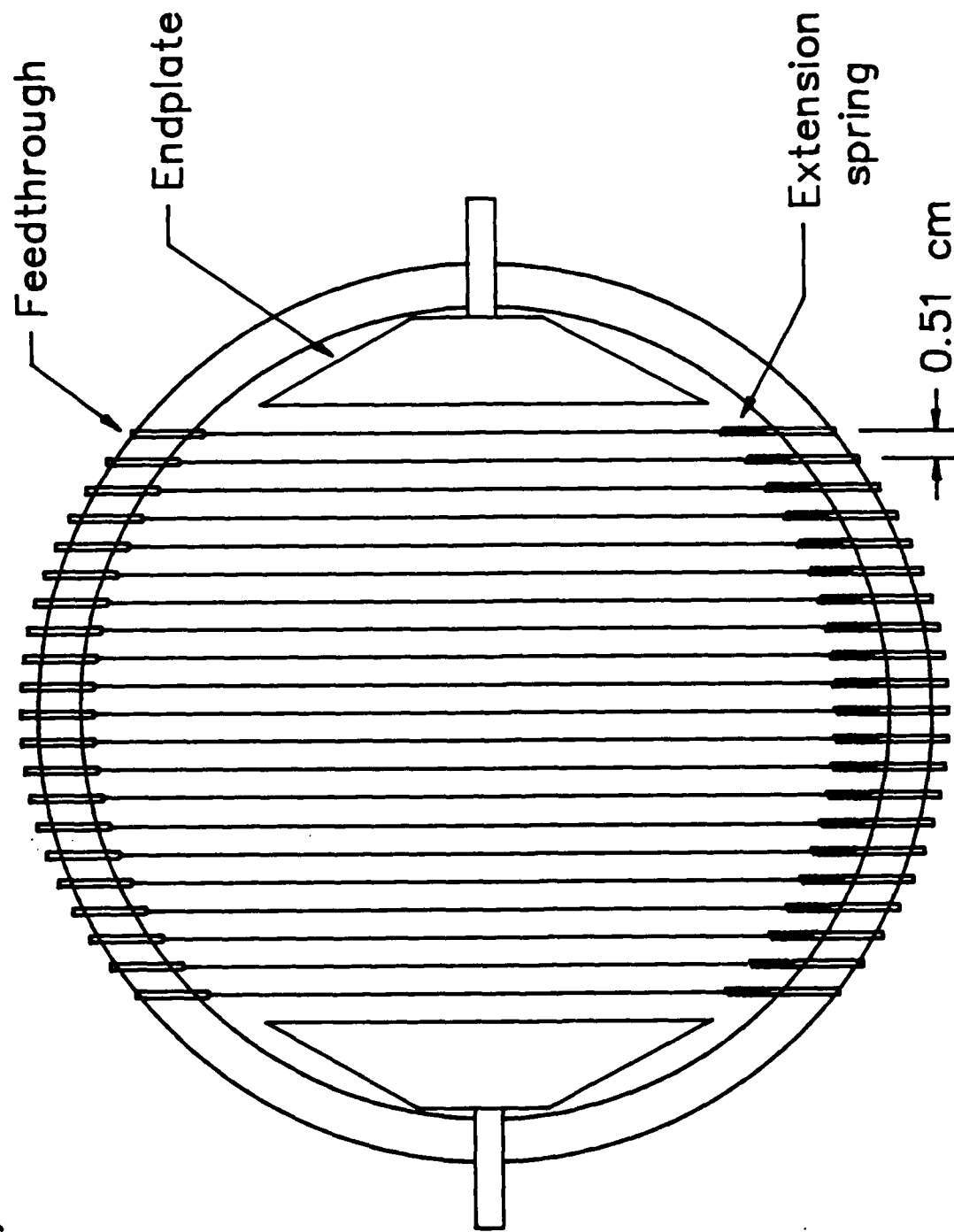




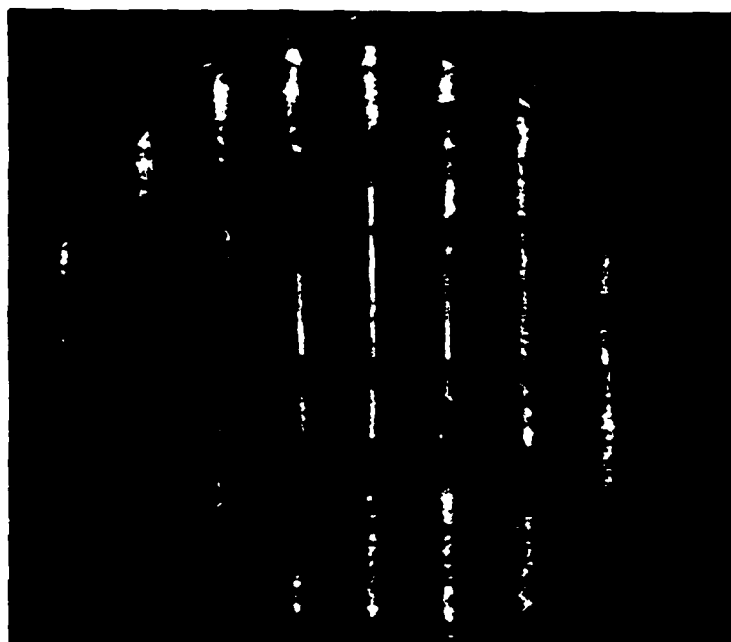
a)



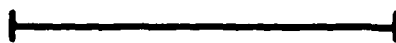
b)



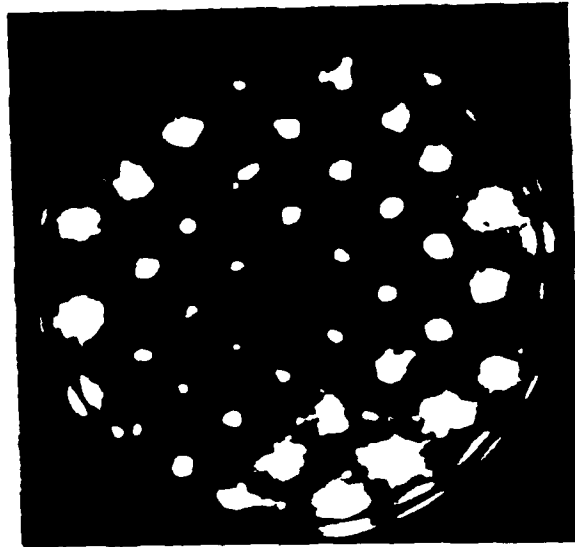
a)



b)



5 cm



5 cm

a)

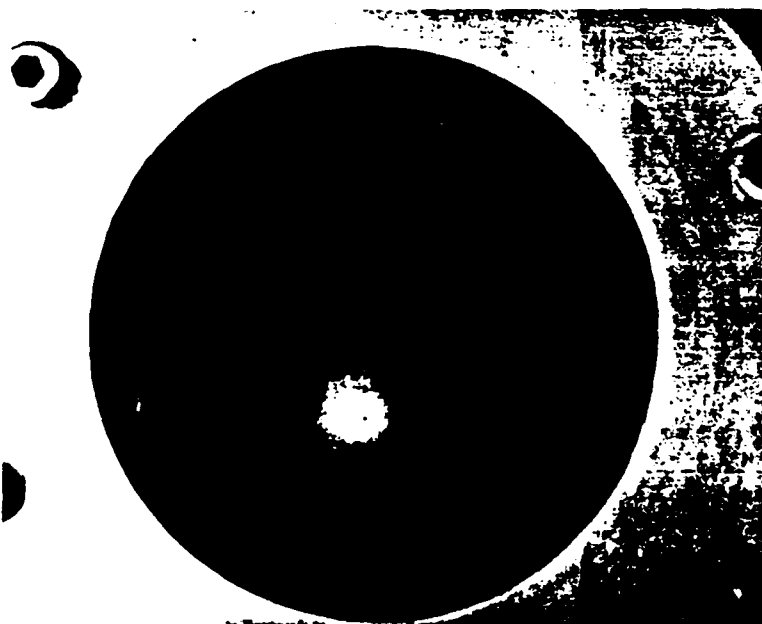


b)



5 cm

c)



Humphries 10(d)

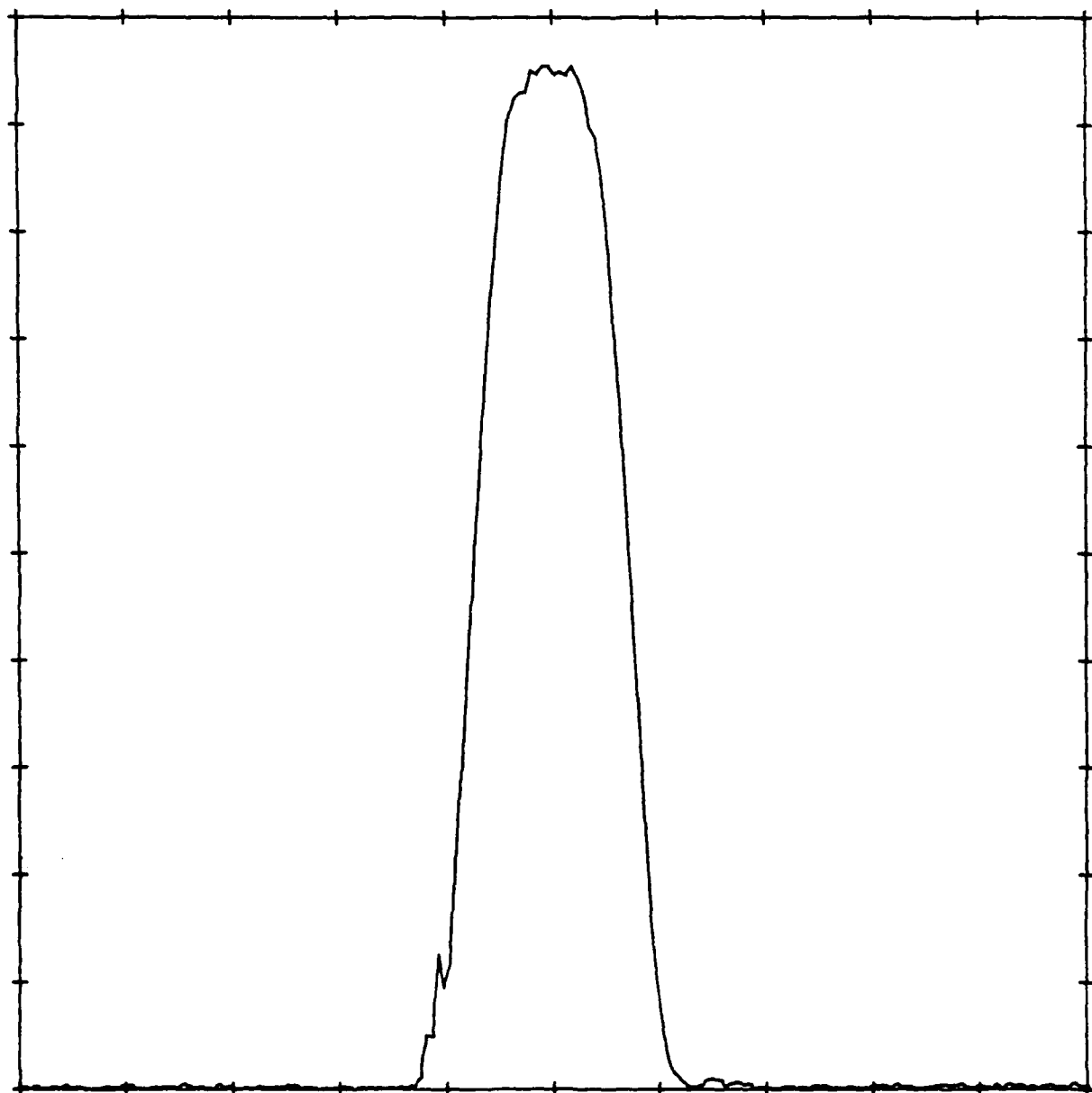
d)

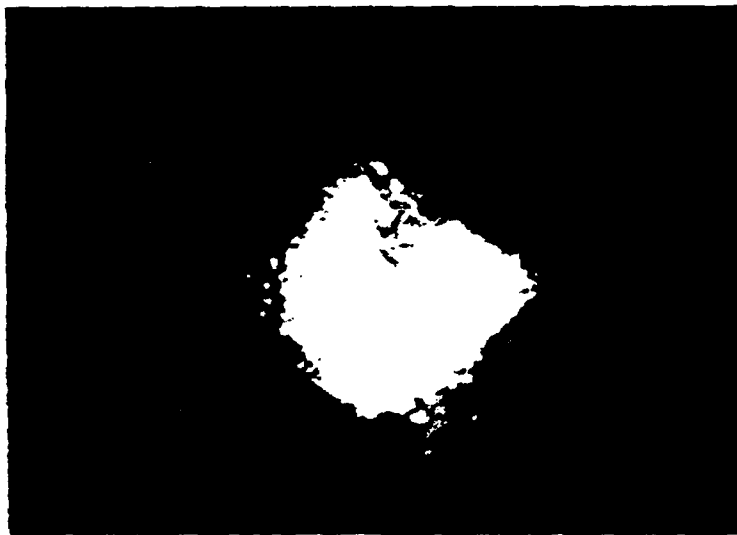
Relative intensity

0.0

Displacement (cm)

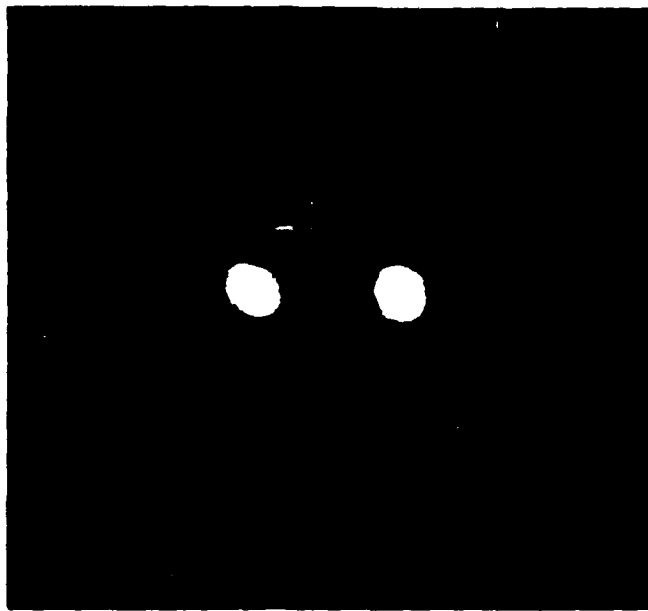
5.0



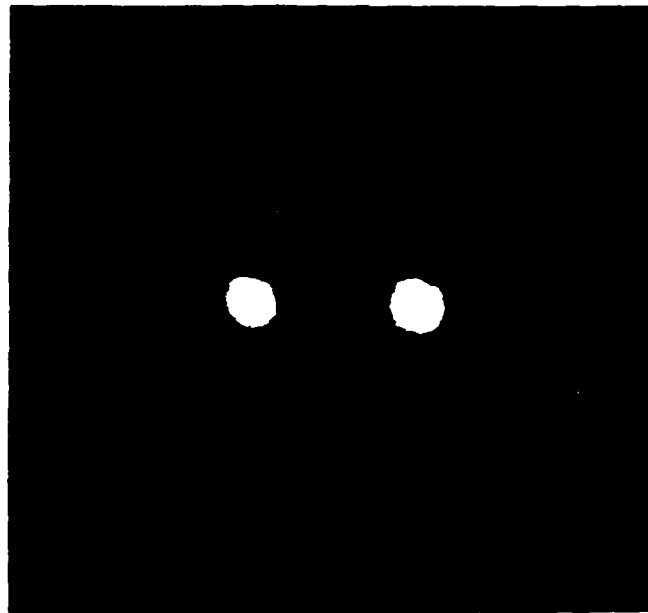


5 cm

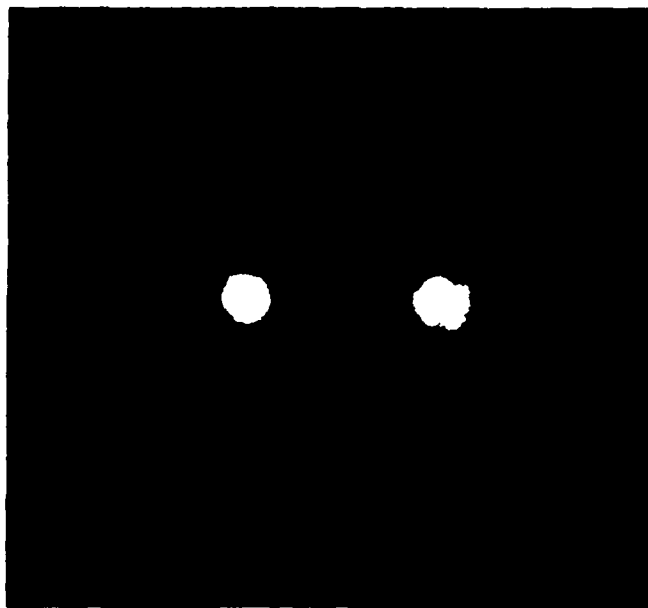
a)



b)



c)



5 cm

Experiments on a Space-charge-corrected Solenoid Lens

-Stanley Humphries, Jr. and R.L. Terry
Department of Electrical and Computer Engineering
University of New Mexico
Albuquerque, New Mexico 87131

1. INTRODUCTION

This paper describes experiments on trapped, non-neutral electron distributions for the correction of spherical aberration in a solenoidal lens. The idea was originally suggested by Gabor for application to electron microscopes [1,2]. Although we have shown that space-charge correction is impractical for electron beam focusing [3], it may have application to negative ion beams. The focusing of such beams has been a subject of recent interest because of potential applications to space-based defense systems [4,5].

References [3] and [6] summarize the motivations for and the projected parameters of corrected solenoidal lenses for negative ion beams. The references also describe our previous experiments using a simple lens with a low-energy electron beam to sample space-charge electric fields. The present paper reports initial experiments on an advanced space-charge lens for ion focusing. The lens volume, applied magnetic field, and space-charge-generated electric field are in the range of interest for high energy ion-beam focusing. The device has twelve sets of electrodes that can be biased individually for fine control of

the space-charge potential.

The experiments concentrated on measurements of the trapped electron distribution in the lens. We used probe arrays to measure the axial and radial variations of the space-charge potential. Capacitive probes measured gross motion of the electron distribution caused by the diocotron instability [7]. For an applied magnetic field of 0.075 tesla, the electron space-charge controlled radial fields up to 40 kV/m. The level of oscillating electric fields associated with the diocotron instability was only about one per cent of the steady-state electric field.

Section 2 describes the principle of space-charge correction of a solenoidal lens and the characteristics of the new apparatus. Section 3 summarizes measurements of the spatial variation of space-charge potential. Section 4 describes measurements of time-varying electric fields resulting from instabilities of the electron distribution. Implications of the results are reviewed in Section 5. Although we found that lens correction is feasible, the application of space-charge corrected lenses is marginal for the demanding requirements of space-based neutral-beam accelerators.

2. EXPERIMENTAL APPARATUS

Figure 1 shows the geometry of the space-charge lens. The device was composed of an axial array of electrically isolated stainless steel ring electrodes with 0.18 m inside diameter.

Acrylic spacers separated the electrode assemblies. The vacuum chamber consisted of stacked acrylic and stainless steel rings with O-ring seals. The ring electrodes defined a reentrant geometry - no magnetic field line that passed through the gap between the electrodes connected to the insulators. The geometry inhibited electron transport to the insulator surfaces. Each ring had a high-current vacuum feedthrough for the operation of electron-emitting thermionic filaments. One end of the lens was connected to a vacuum tee and a cryopump. A vacuum flange at the other end incorporated vacuum feedthroughs for diagnostic signals and a 0.3 m vacuum translator for axial translation of diagnostics. The magnet coil was 0.28 m in diameter and 0.28 m in length. The coil was pulsed with a risetime of 15 ms, much longer than the magnetic penetration time of the metal rings. The peak field in most experiments was 0.075 tesla. Figure 2 shows computed surfaces of constant magnetic flux in the lens volume.

The principle of the space-charge corrected lens is straightforward. The electrode rings have bias potentials with increasing magnitude proceeding from the system ends toward the midplane. The distribution of electrostatic potential is symmetric about the midplane. The axial electric field pulls electrons from thermionic sources mounted on the ring electrodes. The electrons flow along field lines to create a non-neutral distribution within the solenoidal field. Electron flow cancels the component of parallel electric field - as a result, a magnetic field line defines an equipotential surface []. The electrons are confined axially by the applied electric fields and

radially by the magnetic field of the lens. The applied axial electric field expels ions. Within the lens, the electrostatic potential increases radially, providing a defocusing electric force for negative ions. The idea is to adjust the potentials of the rings to achieve a variation of defocusing force that counteracts the non-linear component of the lens magnetic force. In this way, the space-charge electric fields reduce spherical aberration in the lens. Correction of spherical aberration with negatively charged electrons is not possible for positive ions. Reference [3] shows that space-charge lenses are practical only for negative ions or for highly relativistic electron beams.

The lens system was designed so that we could operate electron sources on all sets of ring electrodes. In the present experiments, we used only one source because of equipment limitations. We divided the electrodes into the three groups shown in Fig. 3. All members of a group were electrically connected. The CENTER group included the long central electrode and rings 9, 10, 11 and 12. The SOURCE group contained rings 6, 7, 8 and 13, 14 and 15. The OUTER group included all other rings and the structures attached to the space-charge lens - this group was always grounded. Ring 14 of the SOURCE group contained an electron-emitting filament around the inner diameter. The filament was a 50 μm diameter tungsten wire supported by eight ceramic insulators 1 mm from the surface of the ring. With no magnetic field, the filament emitted about 1.2 mA of electron current.

Figure 2 shows that the inner magnetic field lines intersected

grounded surfaces. Therefore, we were able to locate a grounded structure on axis without perturbing the electrostatic potential in the lens. Figure 3 shows the diagnostics carrier, a 0.025 m wide aluminum I-beam. A precision vacuum translator moved the sliding carrier for axial sweeps of potential. We used electrostatic probes to measure the space-charge potential. The probes consisted of 2 mm diameter pyrex tubes with an exposed stainless steel wire 1 mm in length (Fig. 4). Our previous experiments [3] showed that the probes did not seriously distort the potential inside the electron distribution. We believe that secondary emission raised the local surface potential of the probe insulator to a value near that of the electron distribution.

The probe was connected to the 1 M Ω input of a digital oscilloscope through a 100 M Ω series resistor. The collected electron current depressed the potential of the exposed probe wire to a space-charge potential near that of the surrounding electrons. Under some circumstances, we could infer potential from a measurement of the probe current. The high series resistance assured that the probes extracted at most a few μ A of electrons. The resistor was incorporated in the probe body close to the sensing element to minimize the response time. The probe risetime was limited by cable capacitance and the 1 M Ω termination to ≥ 0.2 ms. The probes showed long-term changes of potential during the rise and fall of the magnetic field - they could not detect oscillations from the diocotron instability that were in the \sim MHz range. In most experiments, we used an

array of four probes at radii of 0.038, 0.051, 0.065 and 0.072 m with an individual digital channels.

We measured the electric field variations resulting from the diocotron instability with the capacitive probes shown in Fig. 4. The probes were half-cylinders with radius and length equal to 0.025 m. The geometry introduced only a small geometric perturbation in the azimuthal direction. The probes were biased to a DC voltage of -100 V to prevent the collection of stray electrons. The probe signal passed through a bias capacitor to a 1 k Ω oscilloscope termination - cable capacitance limited the response time to $\geq 0.1 \mu\text{s}$.

Fig. 5 shows the time-variation of magnetic field (solid line) measured at the midpoint of the lens. The plot also shows the current emitted from the filament. With no magnetic field, all electrons emitted from the filament were drawn to the center electrodes. With electron trapping by the rising magnetic field, the extracted electron current dropped. At peak field, the leakage current was only 50 μA .

3. MEASUREMENTS OF POTENTIAL DISTRIBUTION

To start, we verified that the electrostatic probes responded correctly to differences in electrostatic potential. We placed four probes at different positions in the space-charge lens and measured the signal current versus bias voltage. For this test, we set $V_{\text{source}} = +200\text{V}$ and $V_{\text{center}} = +600\text{V}$ to pull electrons into

the lens volume. Because of the positive space-charge potential, we applied a positive bias voltage, V_b , to the probes to collect electrons. By varying the bias voltage, we were able to measure the local space-charge potential, $\phi(r,z)$, in two ways and compare the results. When the bias voltage was less than ϕ , the probe collected no current:

$$V_s = 0 \text{ for } V_b < \phi. \quad [1]$$

When the bias voltage was higher than ϕ , we expected that the probe collected sufficient electron current to reduce its voltage close to the space-charge potential. Mathematically, this condition is:

$$V_s = (R_s/R_o)(V_b - \phi), \text{ for } V_b > \phi. \quad [2]$$

The quantity R_s in Eq. 2 is the sensing resistor (1 M Ω) at the oscilloscope and R_o is the series resistance in the probe. With the values $R_s = 1 \text{ M}\Omega$ and $R_o = 105 \text{ M}\Omega$, the potential and signal voltage are related by:

$$\phi = V_b - 105V_s. \quad [3]$$

Fig. 6 shows a plot of the signal voltage at peak magnetic field versus bias voltage for the four probes. The probe marked P4 is inside the field line that connects to the source. Probe P3 is just outside the line, while P2 and P1 are well outside the line toward the end of the system. All probes detected electrons. The electrons sampled by probes P2 and P1 probably migrated against the electrostatic potential through instabilities. Extrapolation of the curves to the axis gives the local potential

according to Eq. 1. Probe P4, in a region of high potential, did not detect electrons except at high bias voltage. The other three probes signals exhibited a breakpoint at potential below that of the source. Using the breakpoint potentials and the functional variation of Eq. 3, we made an optimized straight line fit to the data. The dashed lines in Fig. 6 follow the equation:

$$\phi = V_b - \alpha 105V_s, \quad [4]$$

where $\alpha = 1.6$. The probe response had the correct functional form, although the magnitude differed from the theoretical value by 60 per cent. The discrepancy may arise from perturbations in the electron distribution from the collected probe current. We used Eq. 4 in the following analyses as an empirical calibration.

We expected that the electrostatic potential was constant along a field line connected to an electron source. The electrons flowed along the field line to cancel the component of parallel electric field. A similar process accounts for virtual cathode formation in ion beam diodes [8,9]. The magnetic field gradient has little effect on the electron distribution - in the experiment, the magnetic mirror force was a factor of 10^2 - 10^4 lower than the axial electric force. In the experiment, we also observed electrons on field lines that were not connected to the source. There is no simple way to predict the space-charge potential in this case - it depends on complex processes of electron transport. In the proposed full lens configuration, all field lines in the lens volume connect to active sources for predictable control of the potential .

In initial experiments, we created a potential that increased moving axially toward the lens midplane and radially outward. We set $V_{\text{source}} = +200 \text{ V}$ and $V_{\text{center}} = +600 \text{ V}$. The maximum center voltage was limited by probe insulator breakdown. With a bias voltage of $+700 \text{ V}$, probes collected electrons in all regions. We used Eq. 6 to infer the local potential from the probe signals. Fig. 7 shows an axial scan of potential at the peak magnetic field. Data are included for probes at four radial positions. At the midpoint, $z = 0$, inspection of the field map of Fig. 2 shows that probe P2 was close to the field line that connected to the source. As expected, its signal showed a $+200 \text{ V}$ potential. At $z = 0$, probes P3 and P4 were between the source line and the center electrode - their signals implied that potential increased with radius. As the probes moved from the midplane, their signals were consistent with the hypothesis of an equipotential surface along the magnetic field line connected to the source. The outer probe showed constant potential until it crossed the source layer, shaded in Fig. 2. The signal from this probe increased at large values of z . We believe the increased signal did not result from an elevated potential, but rather from insufficient electron density to maintain the probe potential. We have marked suspect values of potential in Fig. 7 with hollow symbols. Probe P3 was immersed in the electron layer at $z = 0$ - its signal showed a constant drop in potential with increasing z . Similarly, the Probe P2 was always inside the layer and had potential less than $+200 \text{ V}$.

The data of Fig. 7 imply that the space-charge potential with electrons was substantially different from the vacuum potential. Fig. 8 plots the measured radial variation of potential at $z = 0.05$ m along with the theoretical values for the potential variation in vacuum between the grounded diagnostic carrier and the biased rings. In vacuum, the electric fields were strongest near the axis. The trapped space-charge in the lens reduced the radial field near the axis and concentrated it at large radius.

To demonstrate the effect of the ring voltages on the space-charge potential in the lens volume, we made measurements with widely different bias voltages. For example, we set up the ring voltages to create a hollow electron ring with a potential minimum between the axis and the CENTER electrodes. Both the CENTER and OUTER electrodes were grounded, while V_{source} equaled -400V. The resulting axial electric fields attracted electrons near the midplane and repelled electrons near the ends of the lens. Because the fields accelerated electrons out the ends the lens, the probes detected no electrons at axial positions outside the source electrodes. We observed electrons in the region of the electrostatic trap, $-0.23 \text{ m} < z < +0.23 \text{ m}$.

Fig. 9 shows axial variations of potential. We set the probe bias voltage to zero because the space-charge potential was negative at all positions. The inner probe at $r = 0.051$ m showed an almost constant negative potential with magnitude below the source potential. The sharp drop-off at 0.1 m resulted from reduced electron density outside the field lines connected to the source. The trace for the 0.064 m probe has interesting features.

The magnitude of the negative potential was low near the midplane, rose to -400 V as the probe crossed the plane defined by the source magnetic field lines, and then dropped sharply as the probe moved outside. The probe at 0.076 m showed similar behavior.

Figure 10 illustrates the radial variation of potential for the data of Fig. 9 - the radial profile is quite different from Fig. 8. There is region of negative potential that follows the shape of the magnetic field line connected to the electron source. Fig. 10 plots the radial variation of potential at three axial locations. The distribution of potential indicates the presence of an annular unneutralized electron ring. With no electrons, the potential near the lens midplane is almost zero at all radii.

The probe measurements imply the electron space-charge sustained radial electric fields greater than 20 kV/m in a 0.075 tesla magnetic field. The potential variation with trapped electrons was significantly different from the vacuum values. The present experiment showed that we could exert control over the potential distribution inside the lens by changing the voltage of the rings.

4. STABILITY MEASUREMENTS

A major issue for the feasibility of space-charge corrected lenses is the stability of the electron distribution. Time

varying electric fields could degrade the emittance of an ion beam passing through the lens. Annular distributions of electrons in long solenoids or magnetic mirrors are unstable to the diocotron instability [10-13]. Here, the radial variation of electric field causes a shear in the electron drift velocity. When viewed in a frame-of-reference rotating at the average electron drift velocity, the electron distribution consists of counter-streaming components. The electron streams are subject to a cross-field two-stream instability. The diocotron instability creates clumps of electrons that rotate at the average electric drift velocity. The instability is strong for a non-neutral electron cloud in a magnetic mirror. The resulting azimuthal electric field components cause radial electron drifts. An annular electron cloud rapidly spreads to an almost uniform radial distribution. In our previous experiments in the solenoidal lens field-geometry, we found that we could sometimes achieve stable annular electron distributions. We postulated that the electron distribution was stabilized by electron conduction along magnetic field lines to the source, effectively short-circuiting azimuthal electric fields.

In the present experiments, we measured the amplitude and time-variation of perturbed radial electric fields using capacitive probes inside the annular electron cloud. For a given time-variation of electric field at the probe, δE_r , the expected signal voltage was:

$$V_s = \epsilon_0 2\pi r_p l_p (2\pi f) \delta E_r R_t. \quad [5]$$

In Eq. 5, r_p is the probe radius (0.025 m), l_p is the probe length (0.025 m) and R_t is the termination resistor (1 k Ω) at the oscilloscope. We inferred the average radial electric field within the electron layer, $\langle E_r \rangle$, from measurements of the frequency of the variations δE_r . If the displacements have an $m = 1$ azimuthal variation, then the RF period of the probe signal equals the average drift rotation time for an electron, or:

$$1/f = 2\pi r_e / (\langle E_r \rangle / B_0). \quad [6]$$

We detected no instabilities at the voltage levels used for measurements with the potential probes. Removing the probes from the volume of the electron layer, we were able increase the applied voltages to investigate the diocotron instability. Fig. 11 shows an oscillograph of the probe signal over the pulse time of the magnetic field. The electric field oscillations began soon after the rise of magnetic field. The amplitude grew with the field magnitude and reached a saturation level at the peak of the field. When the field magnitude dropped, there was a sharp transition and the level of electric field oscillations increased by almost an order of magnitude. This phenomenon occurred reproducibly over a wide range of applied voltage. High level instabilities appeared frequently during the magnetic field decay, sometimes began during the field rise, and almost never appeared at the field.

Fig. 12 shows an event where the instability transition occurred during the magnetic field rise, extinguished at the flat-top, and then started again during the decay. This behavior

may have resulted from radial electron transport during the rising or falling field. We expect that axial conduction to short-circuit azimuthal electric fields was effective only if the electron distribution was connected to the electron source. A changing magnetic field caused radial transport of trapped electrons. The falling magnetic field may have moved the electron cloud from the field line that contacted the source. As a result, the isolated electron cloud might be subject to an enhanced diocotron instability. The data in the following analyses were taken during the steady-state magnetic field when the instability level was moderate.

Fig. 13 shows an expanded view of the signal from one capacitive probe. The signal has a strong oscillation component at about 1.3 MHz with superimposed higher order modes. To infer the average electron drift velocity from the measured oscillation frequency, we needed information on the azimuthal variation of the electron cloud displacement. Using the split ring detectors, we were able to show that the major oscillation component was an $m = 1$ lateral displacement of the electron distribution. Fig. 14 shows oscillographs of summation and difference signals the split ring detectors. Fig. 14a is a difference signal - it has a maximum amplitude when the signals are 180° out of phase. Fig. 14b is a summation signal that has minimum amplitude for out-of-phase signals. The level is greatly reduced in Fig. 14b, verifying that an $m=1$ perturbation accounts for a large fraction of the signals. The residual level in the lower photograph is consistent with the higher order modes visible in Fig. 13. In the

following analyses, we used time-resolved data like that of Fig. 13 to measure the frequency and amplitude of the fundamental oscillation mode.

Fig. 15 shows scaling of the oscillation frequency versus $1/B_z(0,0)$. The data follows almost a linear variation, consistent with the hypothesis that the period equals the circumference of the electron cloud divided by the $E \times B$ drift velocity. The data of Fig. 16 also support this contention. The figure shows the oscillation frequency as a function of the voltage of the center electrodes for constant magnetic field and source voltage. The radial electric field at the electron layer is roughly proportional to V_{center} . We can combine the data of Fig. 16 with the formula:

$$E_r = 2\pi R_s B f, \quad [7]$$

to infer the average radial electric field within the electron layer. In Eq. 7, R_s is the average ring radius, B is the average magnetic field, and f is the oscillation frequency. From Fig. 2 and the potential measurements, we take $R_s = 0.05$ m. The formula predicts an electric field of 38 kV/m at $V_{\text{center}} = +1500$ V, a value consistent with the system geometry.

Fig. 17 shows scaling of the amplitude of electric field oscillations with the radial electric field. The circles show the absolute level of radial field oscillations, δE_r , inferred from Eq. 5. The value rises almost linearly with applied field. The normalized electric field variation, represented by triangles, is almost constant. The average radial electric field, E_r , was

derived from Eq. 7. The plot shows that the amplitude of field oscillations is small compared to the steady-state electric field. For the parameters studied, the maximum value is less than 1 per cent.

5. CONCLUSIONS

The radial electric field supported by bare electron space-charge in the lens was in a range of interest for applications. Reference 6 shows that a radial field of 4 kV/m would be sufficient to correct spherical aberration in a solenoid lens for a 10 MeV research beam. For the high energy beams of interest for space-based neutral particle accelerators, the electric field value should be comparable to 200 kV/m. In the present experiments, the electric fields in the lens are within a factor of five of this level. Although the full system was not operational, the experiments imply that the external ring potentials control the space-charge potential of trapped electron distributions that significantly modify fields from the vacuum values. The low level of electric field oscillations and the existence of a non-neutralized annular electric distribution indicate that the diocotron instability has a small effect in the solenoid lens field geometry.

The main feasibility question for the application of space-charge lenses to space-based neutral particle beam accelerators is whether they can achieve the high degree of correction necessary for the application. The aiming error should be on the

order of 1 μ radian. We can make a rough estimate of the implications of the present results. Suppose we have a solenoid used as the output lens of a beam telescope. The solenoid has a 2 m length and radius 0.3 m. From previous calculations of magnetic fields, we expect a non-linear force error of about 2% at the envelope of a beam with 0.25 m radius. If the lens has a 5 m focal length, the net deflection of envelope particles is 50 milliradians. For the given force error, the envelope electrons are overfocused by an angle of -1 milliradian. Therefore, the average radial electric field through the lens volume must be strong enough to produce an angular deflection of +1 milliradian. For 100 MeV ion, the axially-averaged radial electric field is 100 kV/m. Unfortunately, even the small level of fluctuations observed in the experiments extrapolate to angular errors that are an order of magnitude too high for the application. A one per cent field error superimposed on a net deflection of 1 mrad given an angular divergence of 10 μ radians. Although the application of space-charge lenses to space-based neutral particle accelerators appears marginal, the lenses may have application to conventional negative ion beams and highly relativistic electron beams in linear colliders.

This work was supported in part by the Air Force Office of Scientific Research under Contract No. AFOSR-86-0063 and by internal research and development funding from Acceleration Consultants. We would like to thank G. Hess for his help in the initial lens experiments and contributions to the theoretical analysis of space-charge potential.

REFERENCES

1. D. Gabor, The Electron Microscope (Hulton, London, 1945).
2. D. Gabor, Nature 160, 89 (1947).
3. G.Hess and S. Humphries, Jr., J. Appl. Phys. 60, 1569 (1986).
4. R.A. Jameson, "High-brightness H⁻ Accelerators," in Proc. 1987 Particle Accelerator Conference, edited by E.R. Lindstrom and L.S. Taylor (IEEE, No. 87CH2387-9, 1987), 903.
5. R.A. Jameson, "High-brightness RF Linear Accelerators," in High-brightness Accelerators, edited by A.K. Hyder, M.F. Rose and A.H. Guenther (Plenum, New York, 1988), 169
6. G.R. Hess and S. Humphries, Jr., Nucl. Instrum. and Methods A-258, 572 (1987).
7. See, for instance, R.C. Davidson, Theory of Non-neutral Plasmas, (Benjamin, Reading MA, 1974), 66.
8. J.W. Poukey and S. Humphries, Jr., Appl. Phys. Lett. 33, 122, (1978).
9. See, for instance, R.B. Miller, Intense Charged Particle Beams, (Plenum, New York, 1982), 118.
10. J. DeGrassie and J. Malmberg, Phys. Rev. Lett. 39, 1077 (1977).
11. T.M. O'Neill and C.F. Driscoll, Phys. Fluids 22, 266 (1979).

12. T.M. O'Neill, Phys. Fluids 23, 2216 (1980).
13. C.F. Driscoll and J.H. Malmberg, Phys. Rev. Lett. 50, 167 (1983).

FIGURE CAPTIONS

1. Geometry of the space-charge-corrected solenoid lens.
2. Computed surfaces of constant magnetic flux in the space-charge-corrected lens volume. Shaded region shows field lines connected to source electrodes (6,7,8,13,14,15). Dashed lines show path of potential probes during an axial sweep. (Dimensions in inches.)
3. Scale drawing of ring electrodes, the sliding diagnostic carrier, and the electrostatic probe array.
4. Scale drawings of diagnostics. Side-view of potential probe assembly and end-view of split ring capacitive pickups.
5. Magnetic field (solid line) and filament emission current (dashed line) versus time. $V_{\text{source}} = +200 \text{ V}$ and $V_{\text{center}} = +1500 \text{ V}$.
6. Calibration of the potential probes, variation of signal with bias voltage. $V_{\text{center}} = +600 \text{ V}$, $V_{\text{source}} = +200 \text{ V}$, $B(0,0) = 0.075 \text{ tesla}$. Radial positions: P1 (0.038 m), P2 (0.051 m), P3 (0.064 m), P4 (0.076 m).

SP

7. Axial variation of electrostatic potential at four radial positions measured at the magnetic field maximum. $V_{\text{center}} = +600$ V, $V_{\text{source}} = +200$ V, $B(0,0) = 0.075$ tesla. Hollow symbols show regions where electron depletion interferes with measurement.
8. Radial variation of potential at $z = 0.05$ from the data of Fig. 7. Circles: Measured space-charge potential. Squares: Calculated vacuum potential. $V_{\text{center}} = +600$ V, $V_{\text{source}} = +200$ V, $B(0,0) = 0.075$ tesla.
9. Axial variation of electrostatic potential at three radial positions measured at the magnetic field maximum. $V_{\text{center}} = +0$ V, $V_{\text{source}} = -400$ V, $B(0,0) = 0.075$ tesla.
10. Radial variation of potential at three axial locations, from the data of Fig. 9. 8. $V_{\text{center}} = +0$ V, $V_{\text{source}} = -400$ V, $B(0,0) = 0.075$ tesla.
11. Long-term probe signals. Magnetic field at lens center, 5 ms/div, 340 G/div. b) Output from single capacitive probe, 5 ms/div, 0.5 V/div, 1 k Ω termination. $V_{\text{center}} = +1500$ V, $V_{\text{source}} = +200$ V.
12. Transition to high level diocotron instability. $V_{\text{source}} = +200$ V, $V_{\text{center}} = +1500$ V, $B(0,0) = 0.075$ tesla.
13. Capacitive probe output at peak magnetic field. 100 mV/div, 500 ns/div, 1 k Ω termination. $B(0,0) = 0.075$ tesla, $V_{\text{center}} = +1500$ V and $V_{\text{source}} = +200$ V.
14. Combined signals from the split ring probes. a) Difference

Final Report - Beam Optics Test Stand

signal, Probe A - Probe B. b) Summation signal, Probe A + Probe

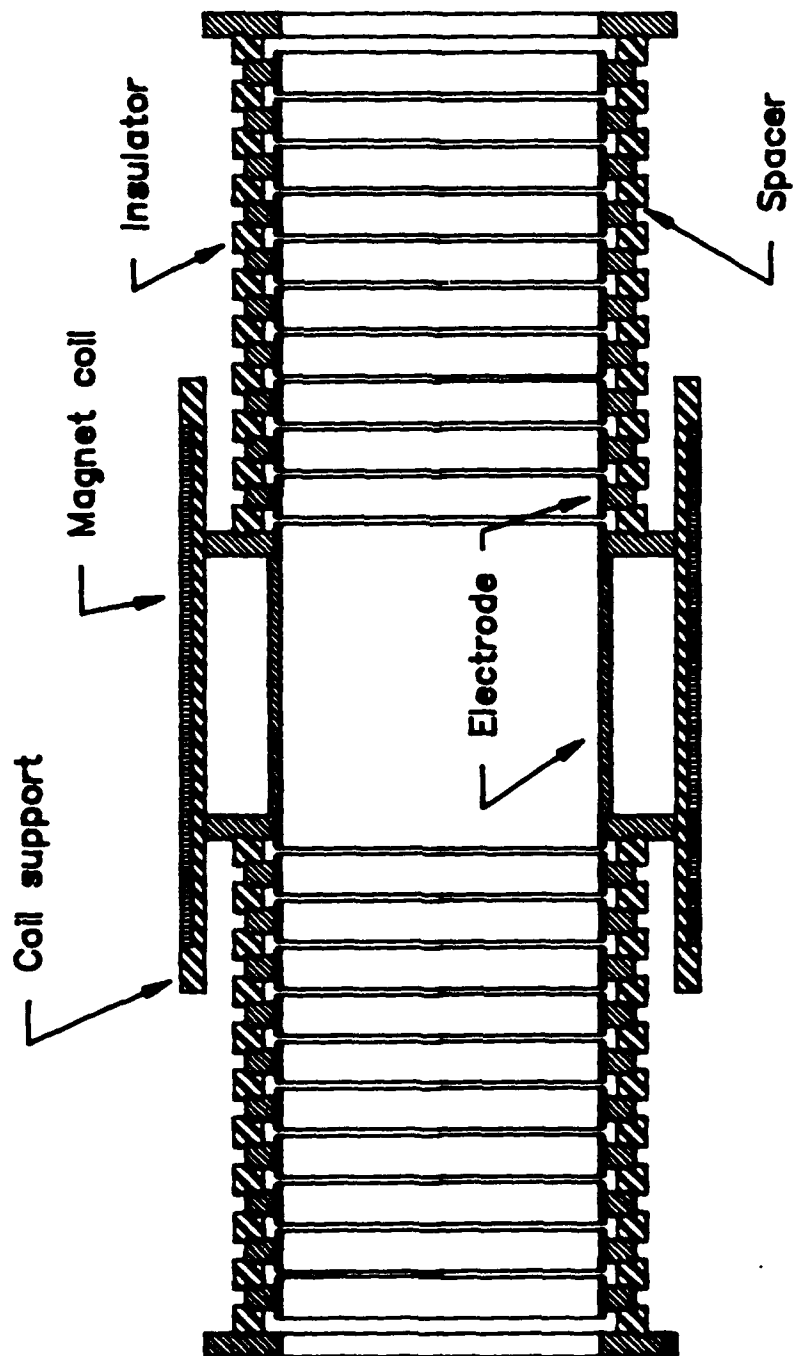
B. $B(0,0) = 0.075$ tesla, $V_{\text{source}} = +200$ V, $V_{\text{ring}} = +1200$ V.

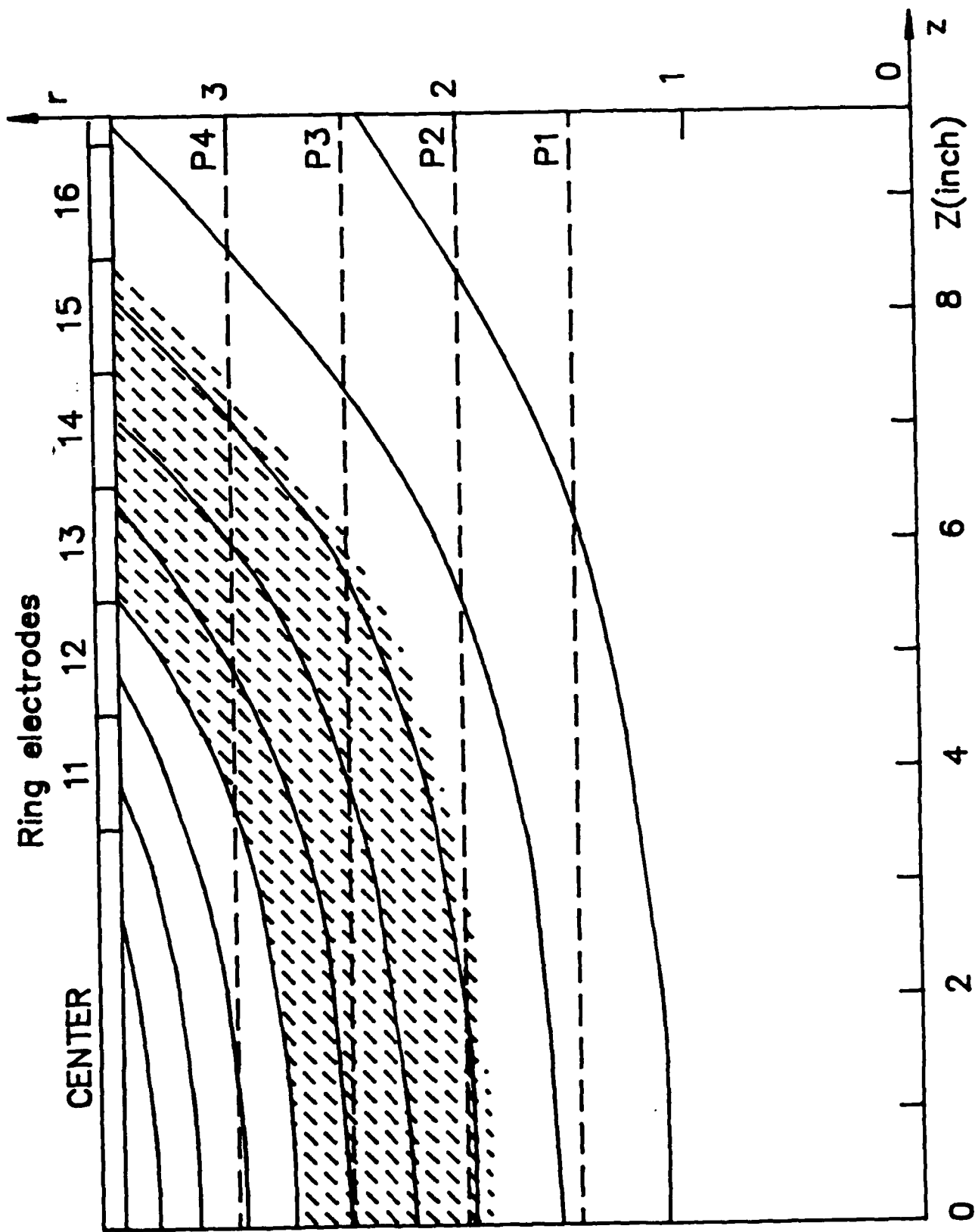
15. Oscillation frequency of $m=1$ displacements versus inverse of magnetic field. $V_{\text{source}} = +200$ V and $V_{\text{center}} = +1200$ V.

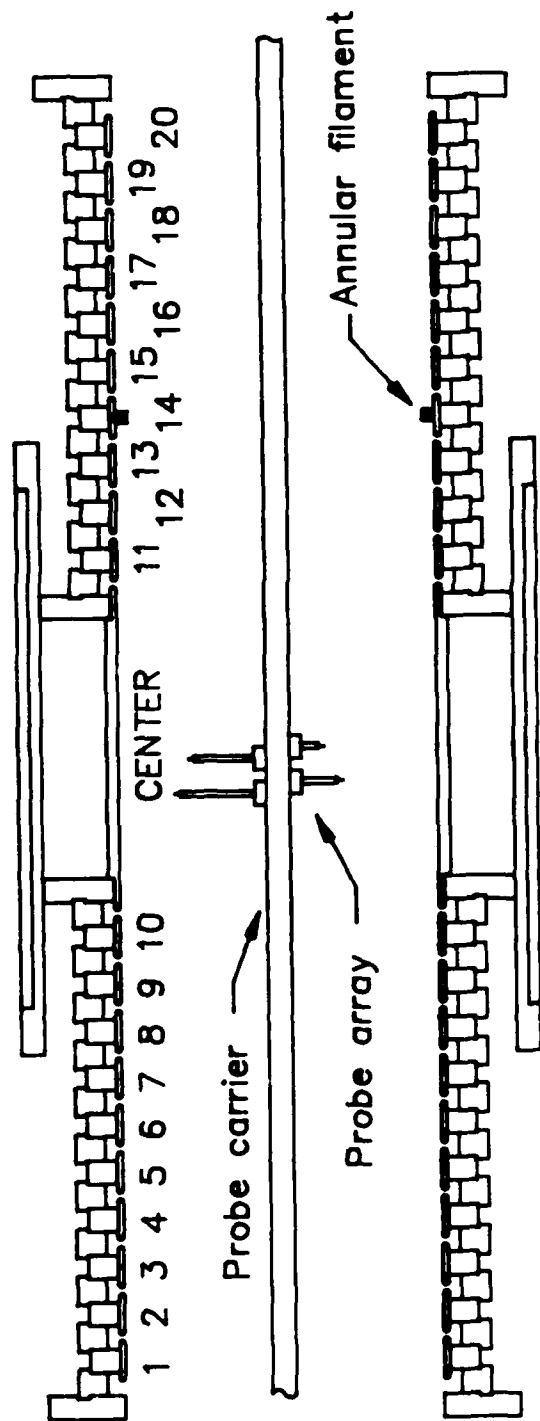
16. Oscillation frequency of $m=1$ displacements versus voltage on center electrode. $V_{\text{source}} = +200$ V, $B(0,0) = 0.075$ tesla.

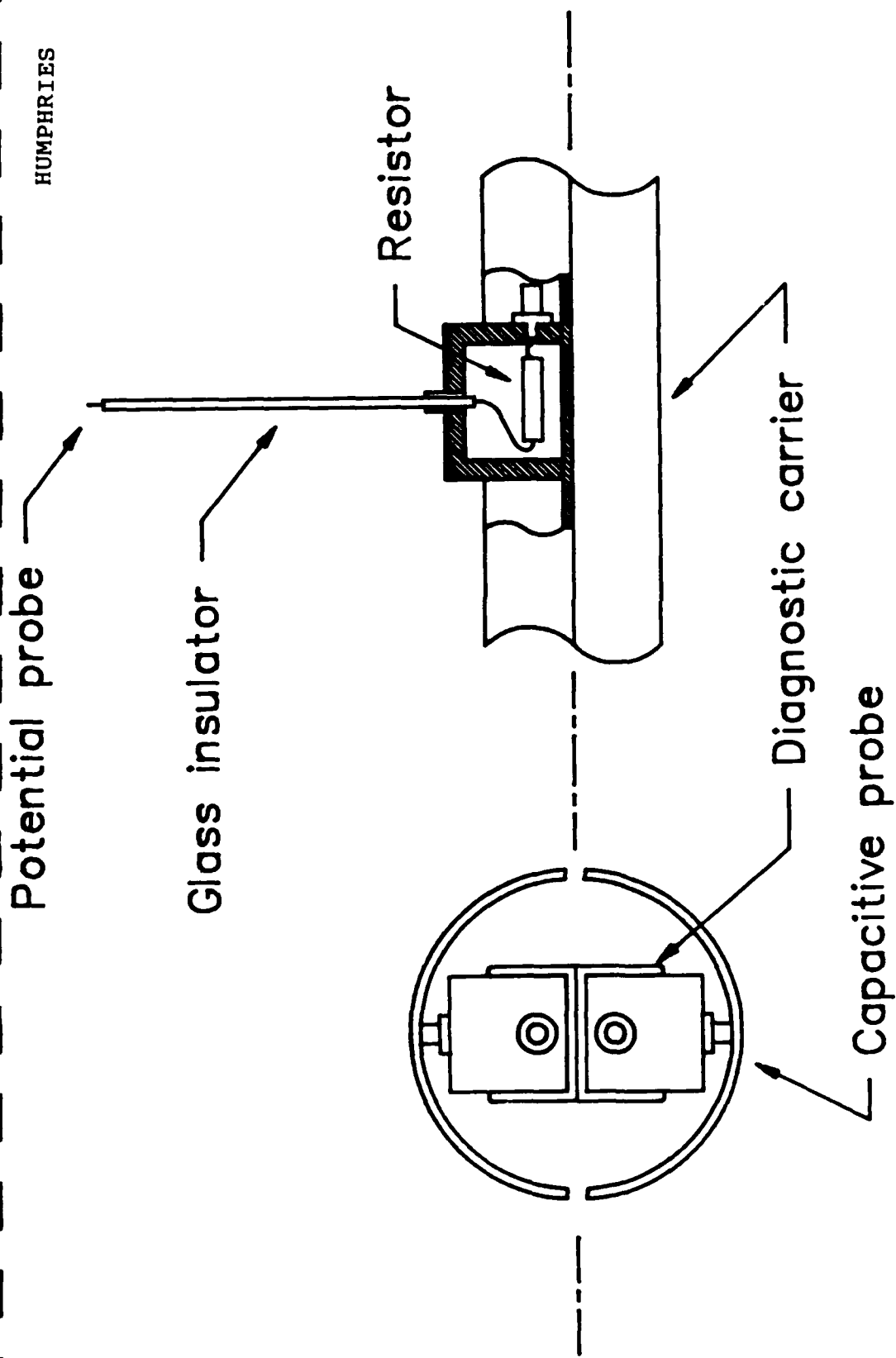
17. Root-mean-squared amplitude of electric field oscillations versus divided by the average radial electric field in the electron distribution as a function of V_{center} . $V_{\text{source}} = +200$ V, $B(0,0) = 0.075$ tesla.

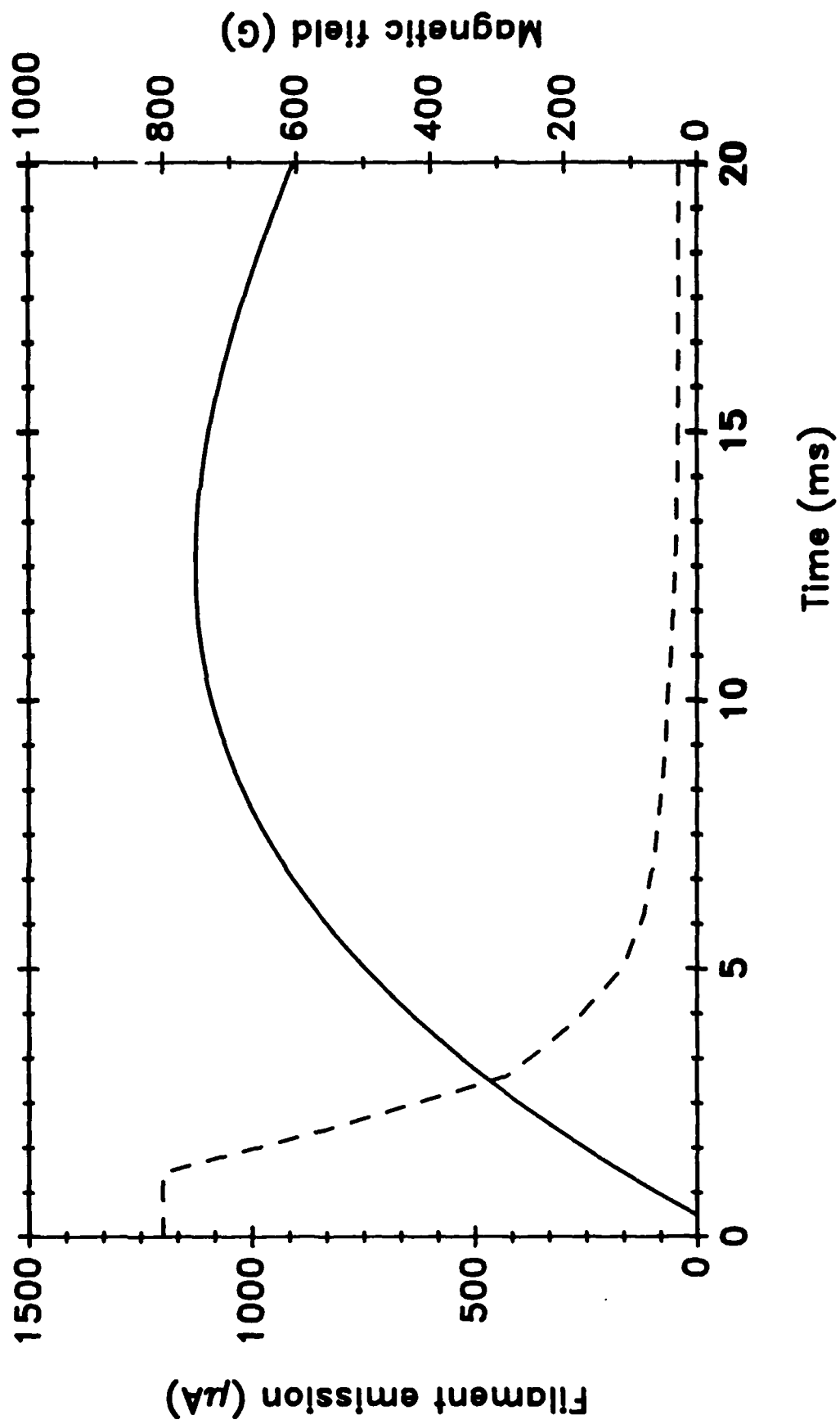
HUMPHRIES 1



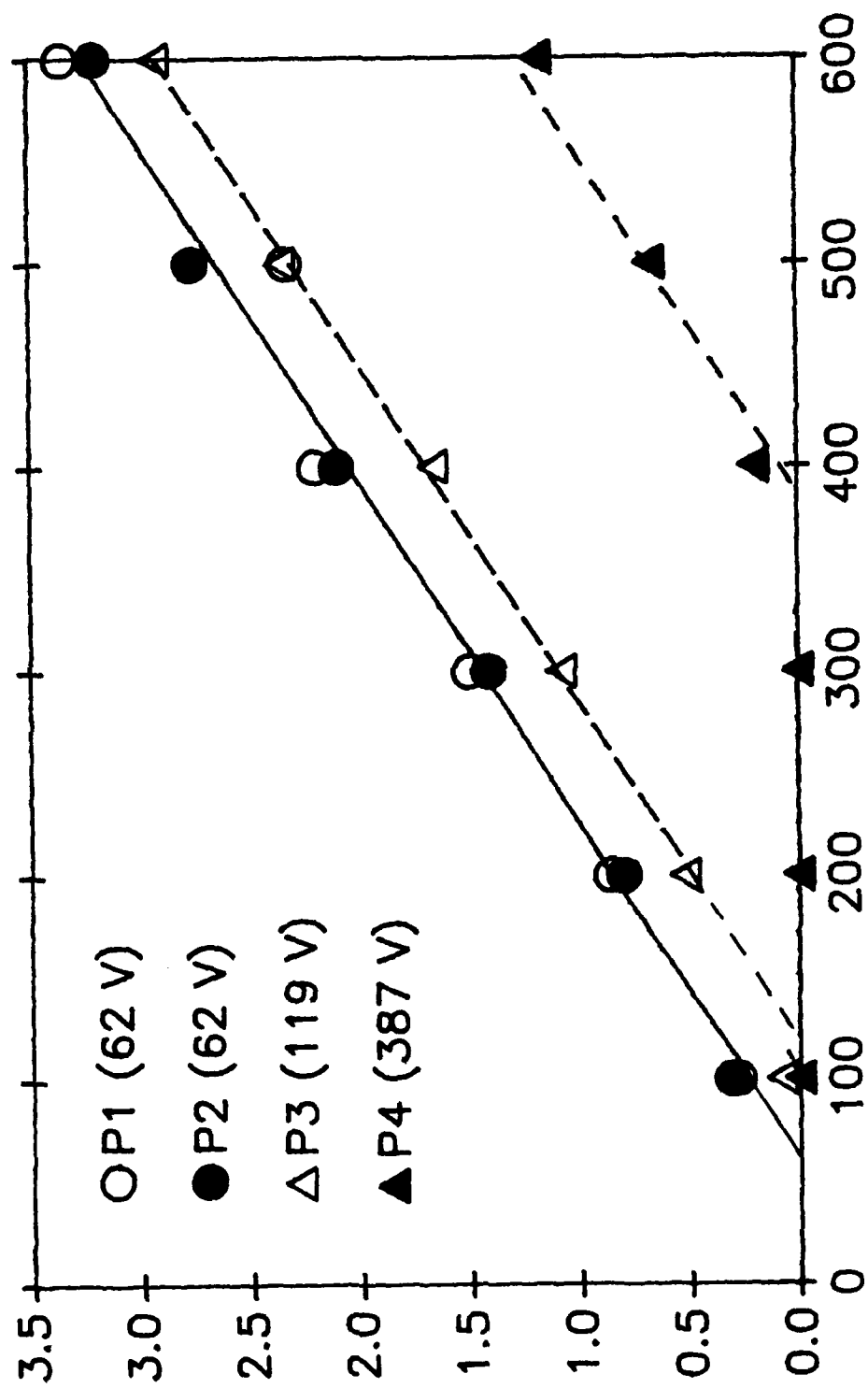


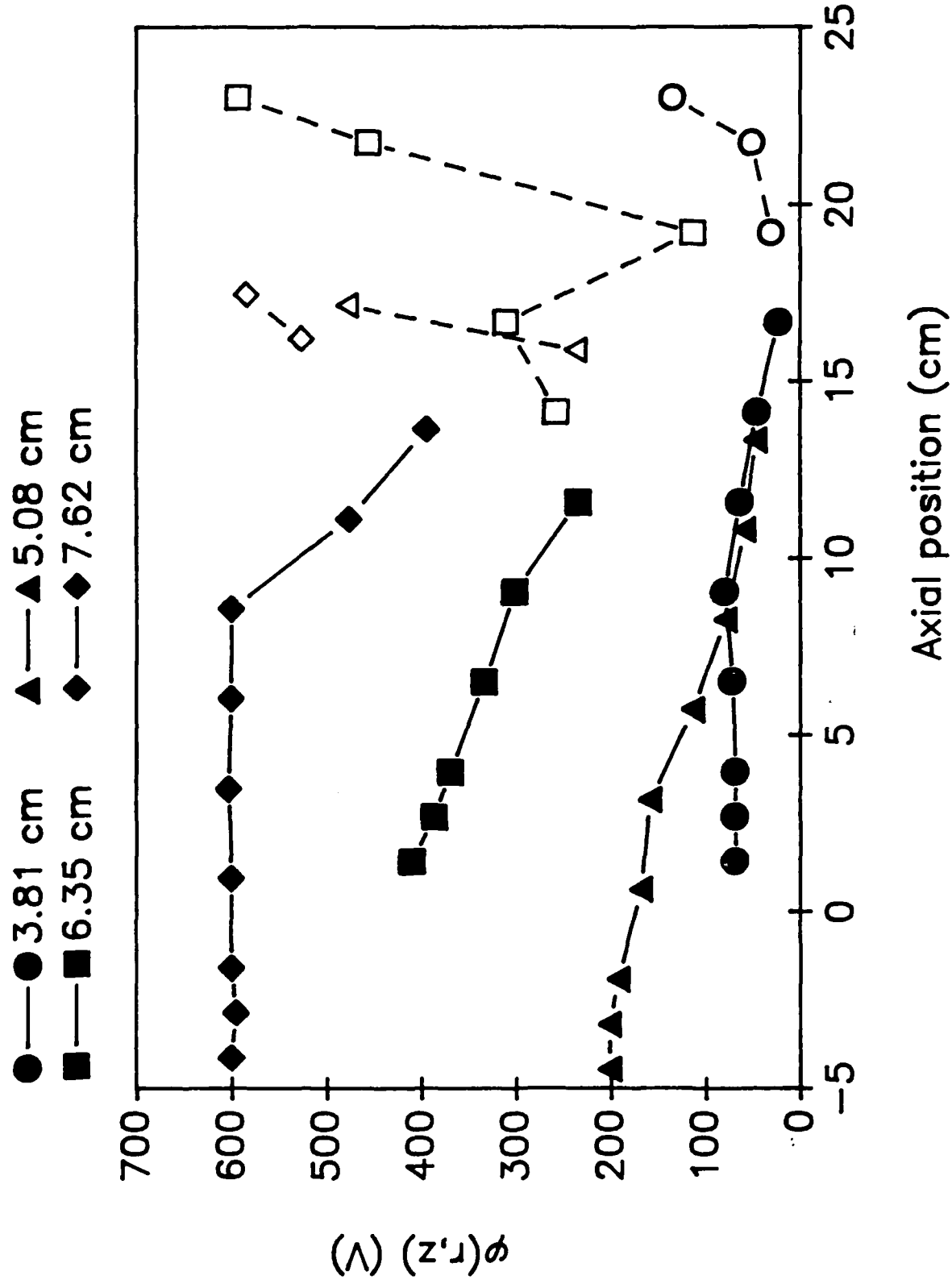


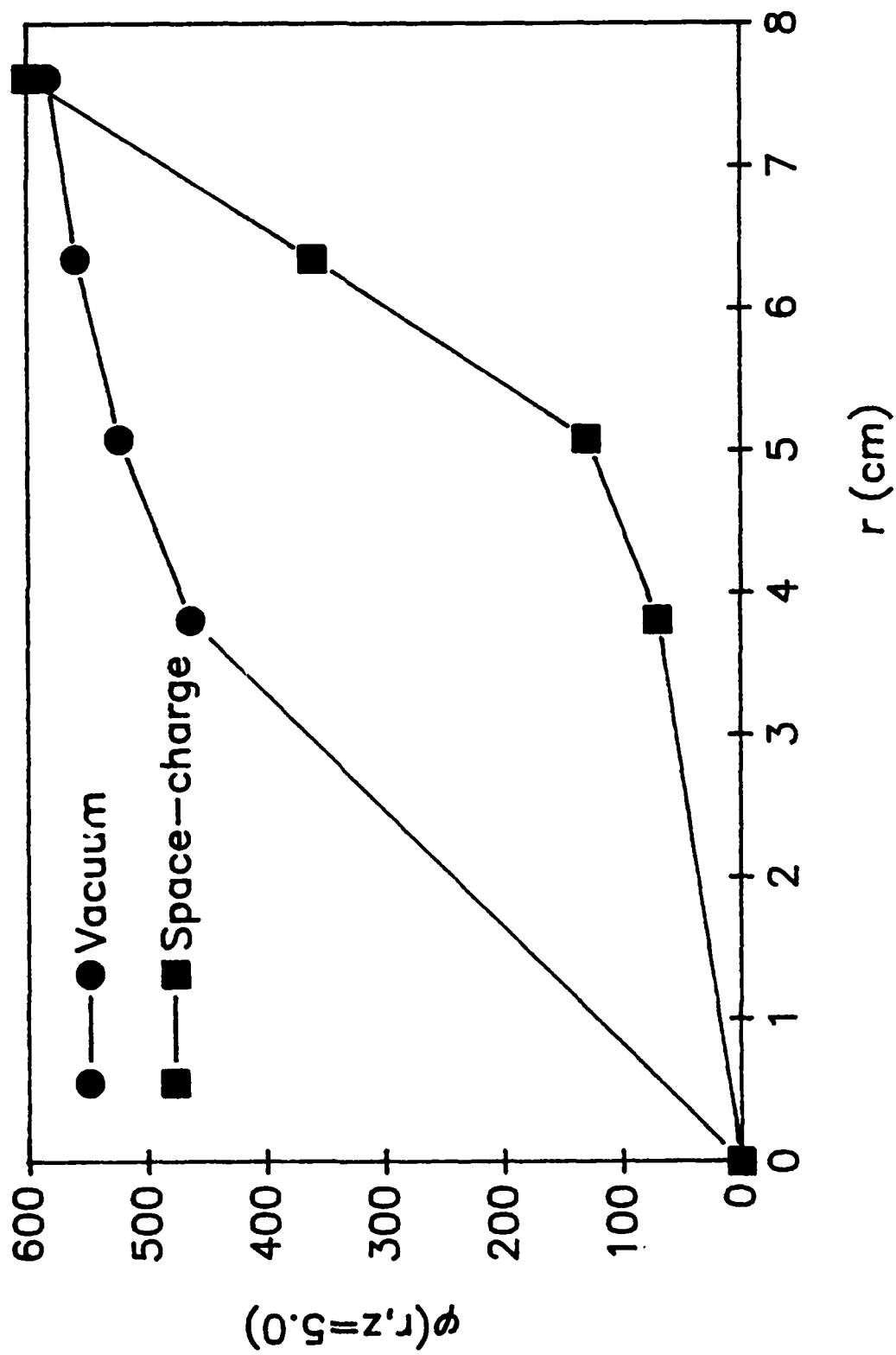


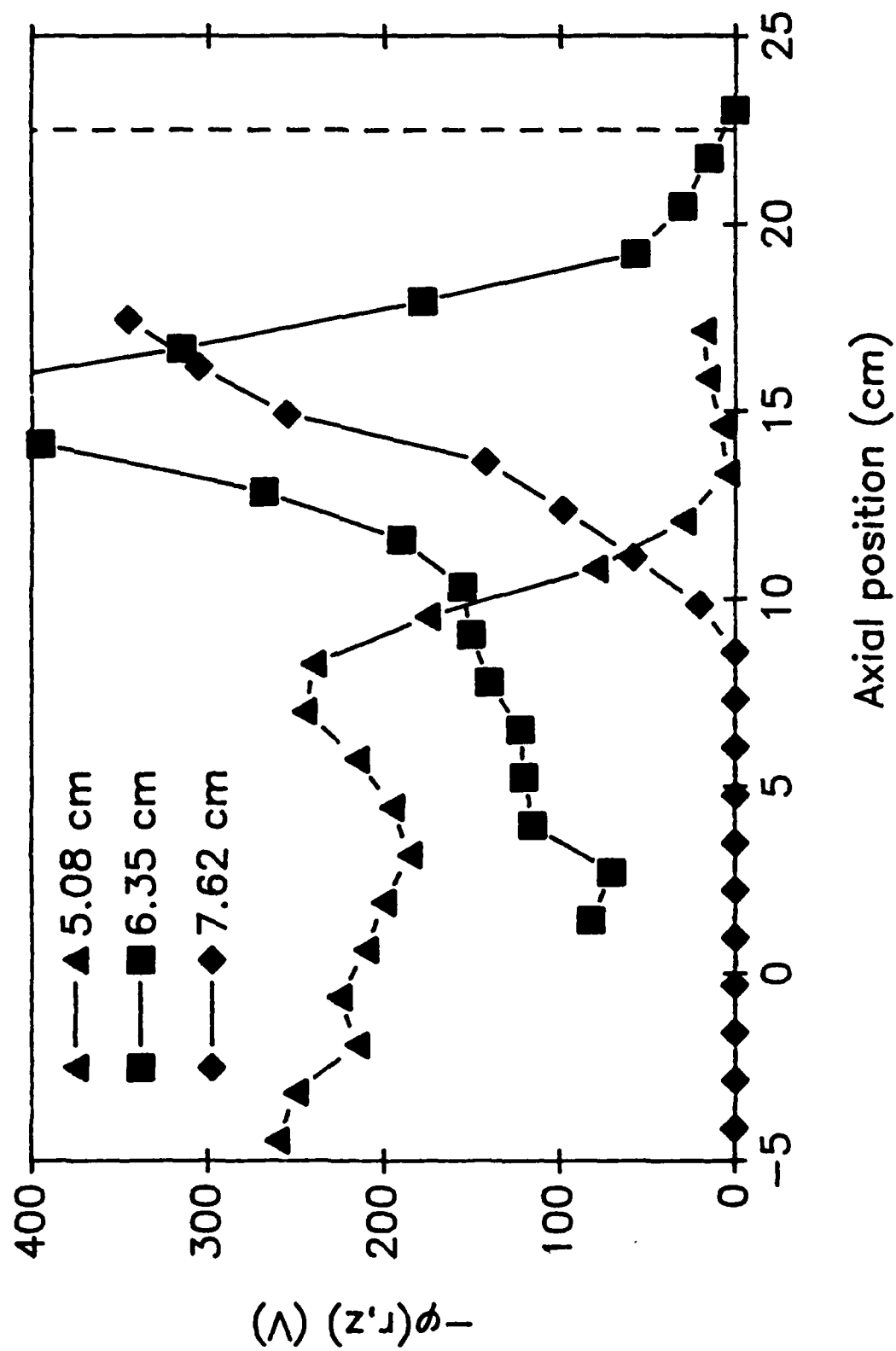


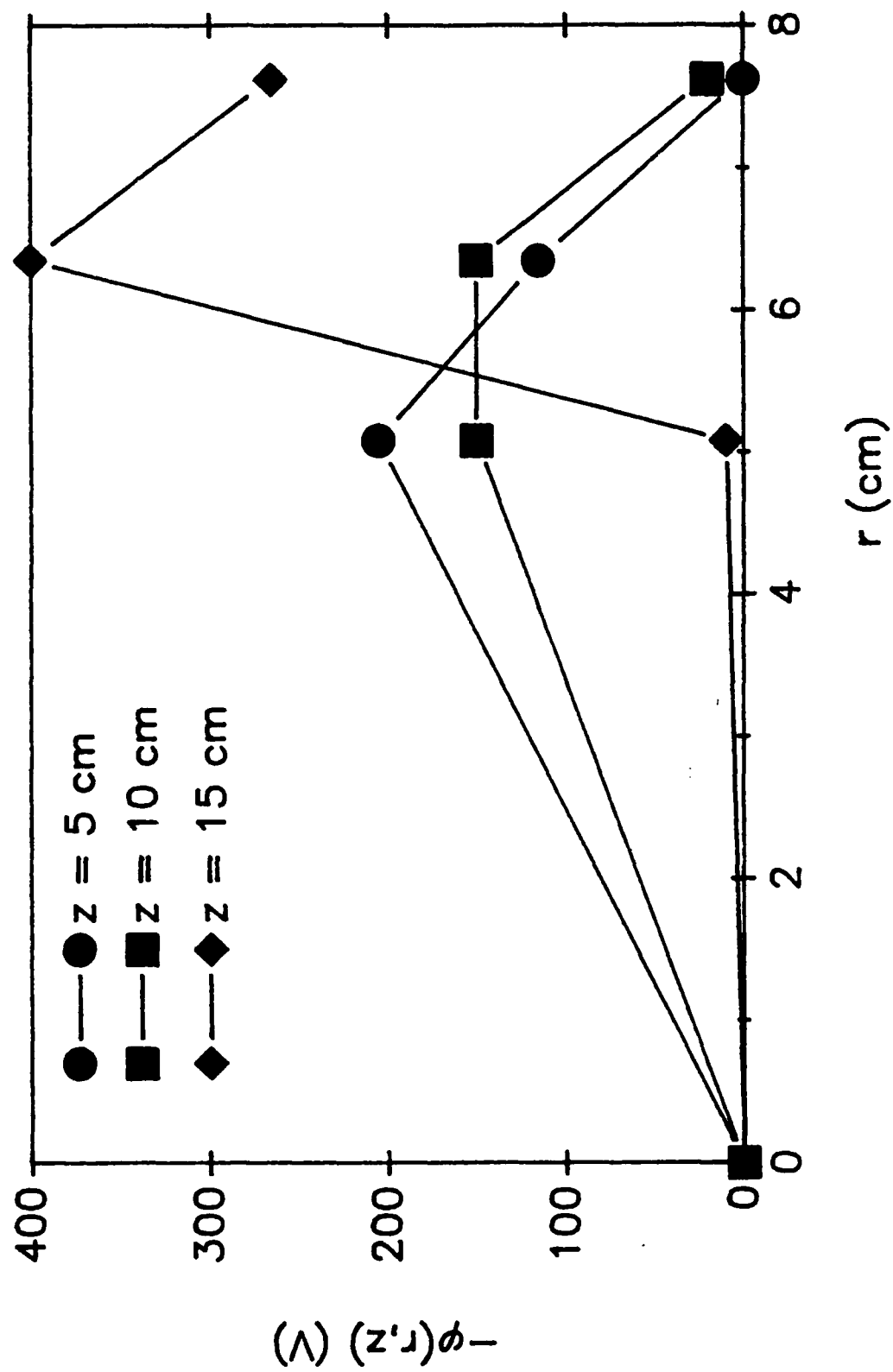
HUMPHRIES 6

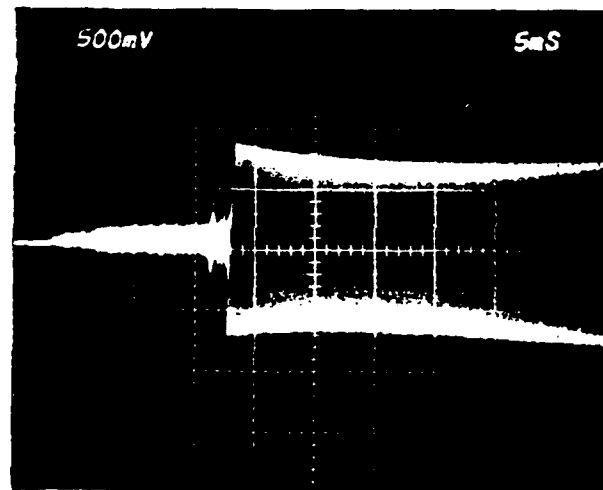
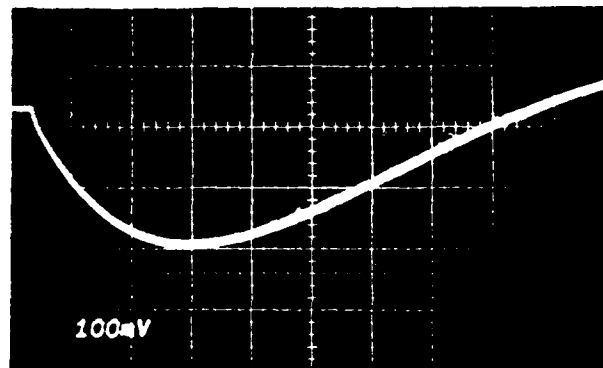




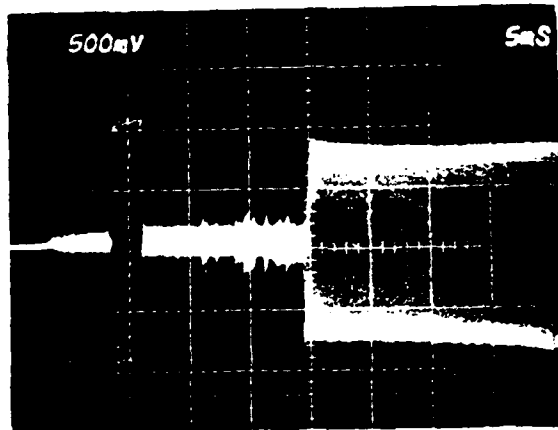




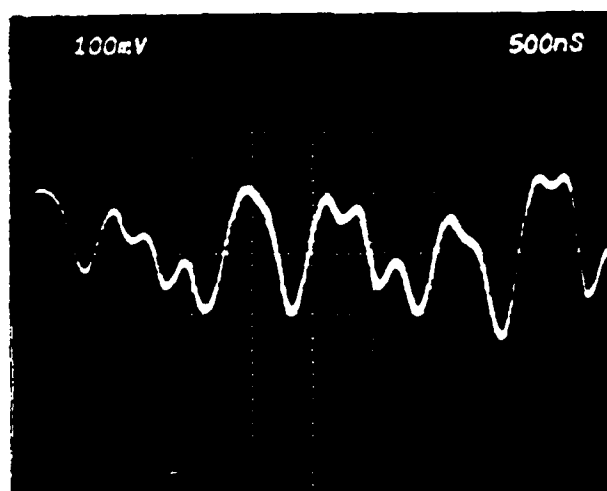


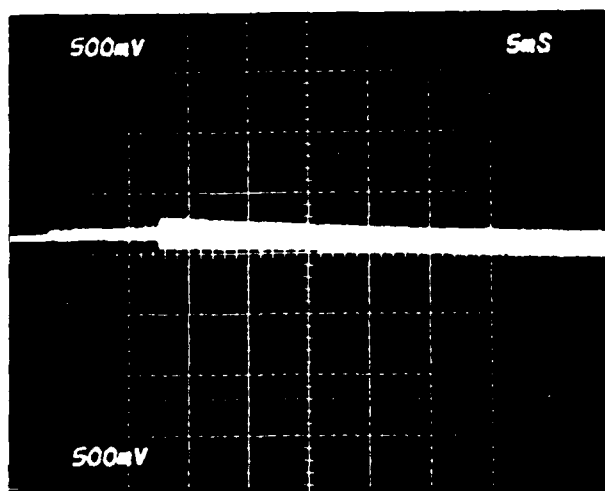
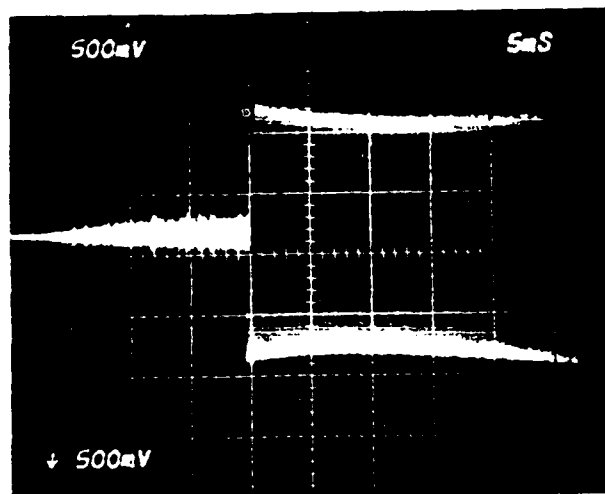


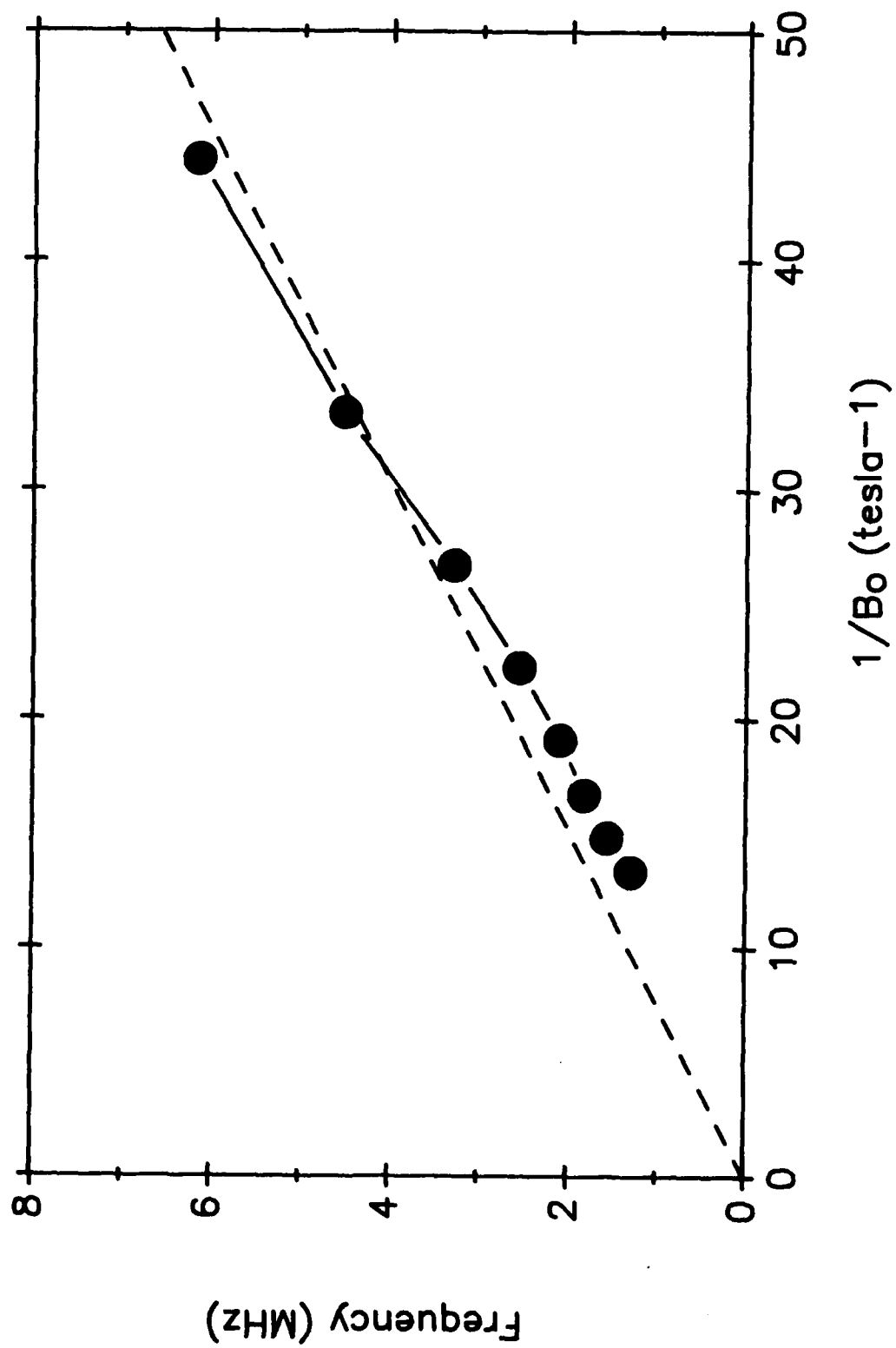
Humphries 12

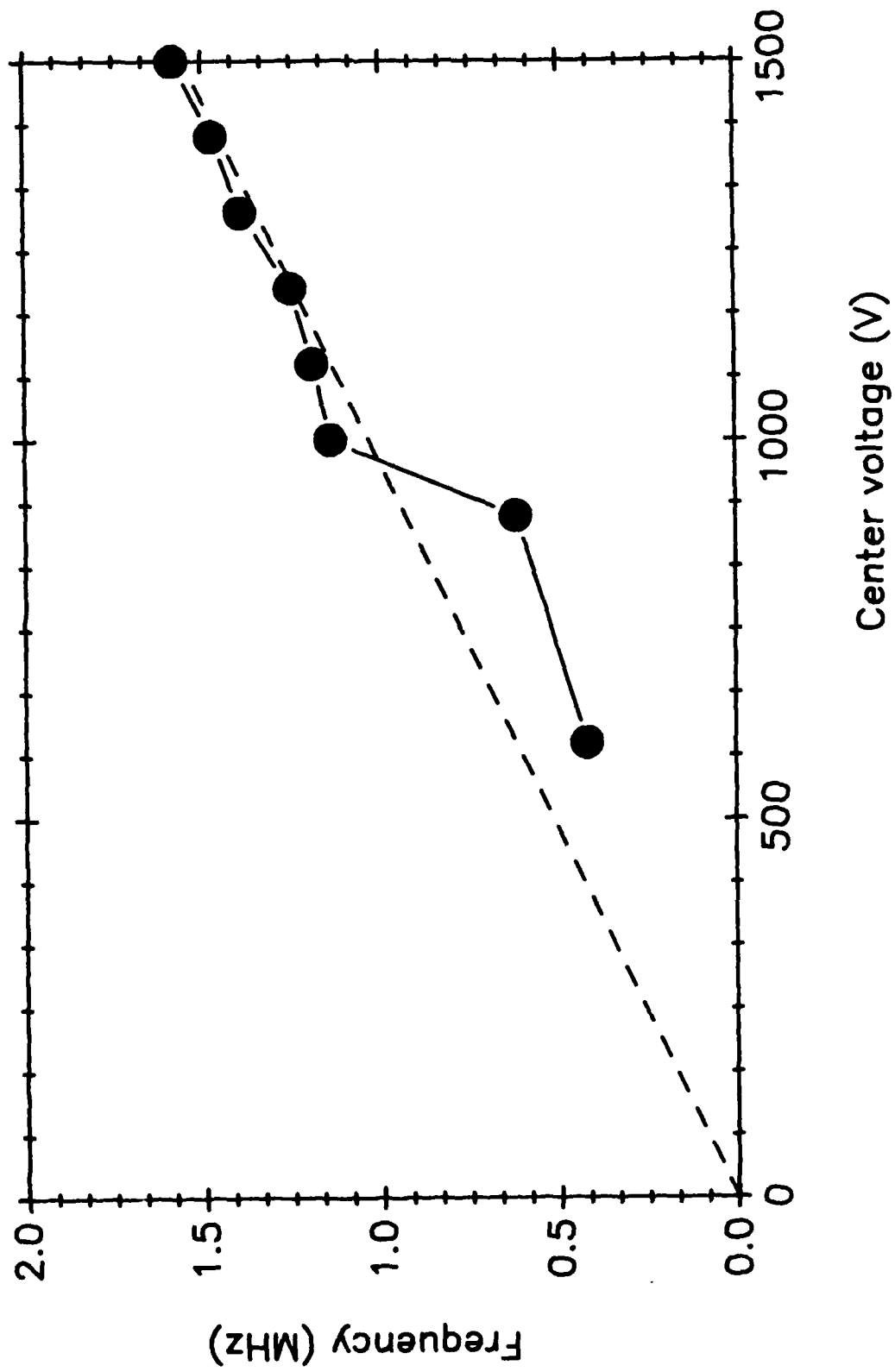


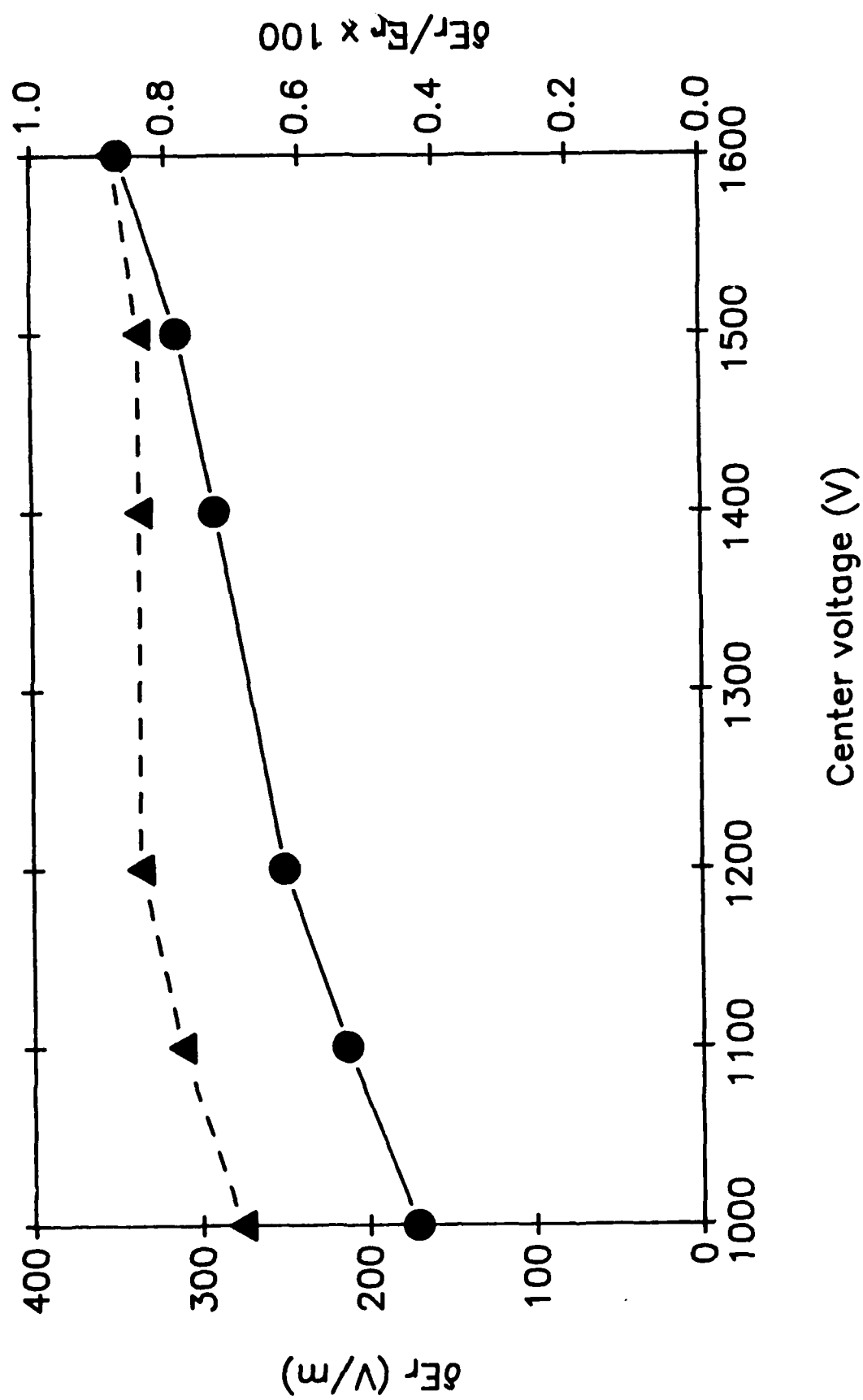
Humphries 13









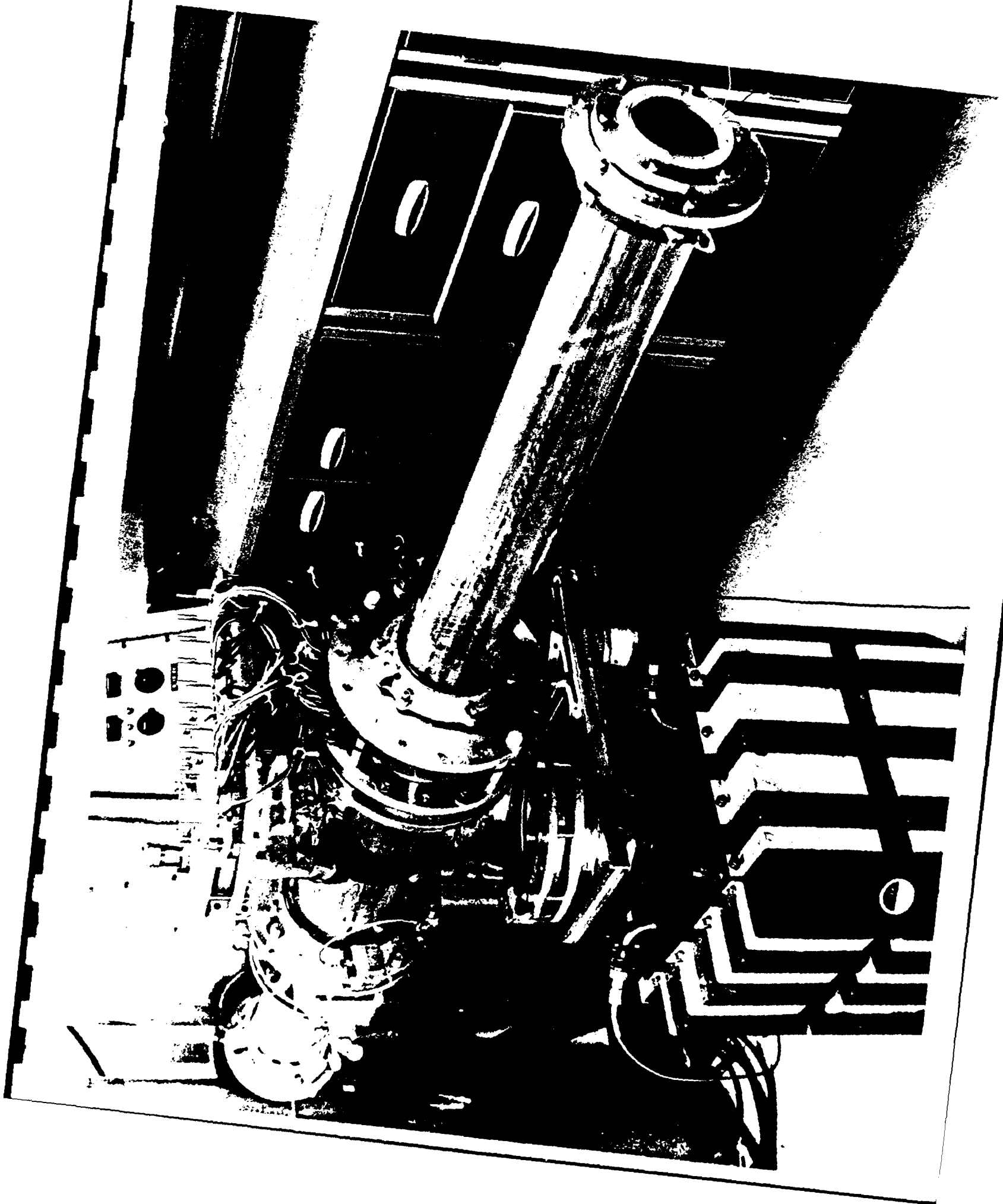


SECTION 4.

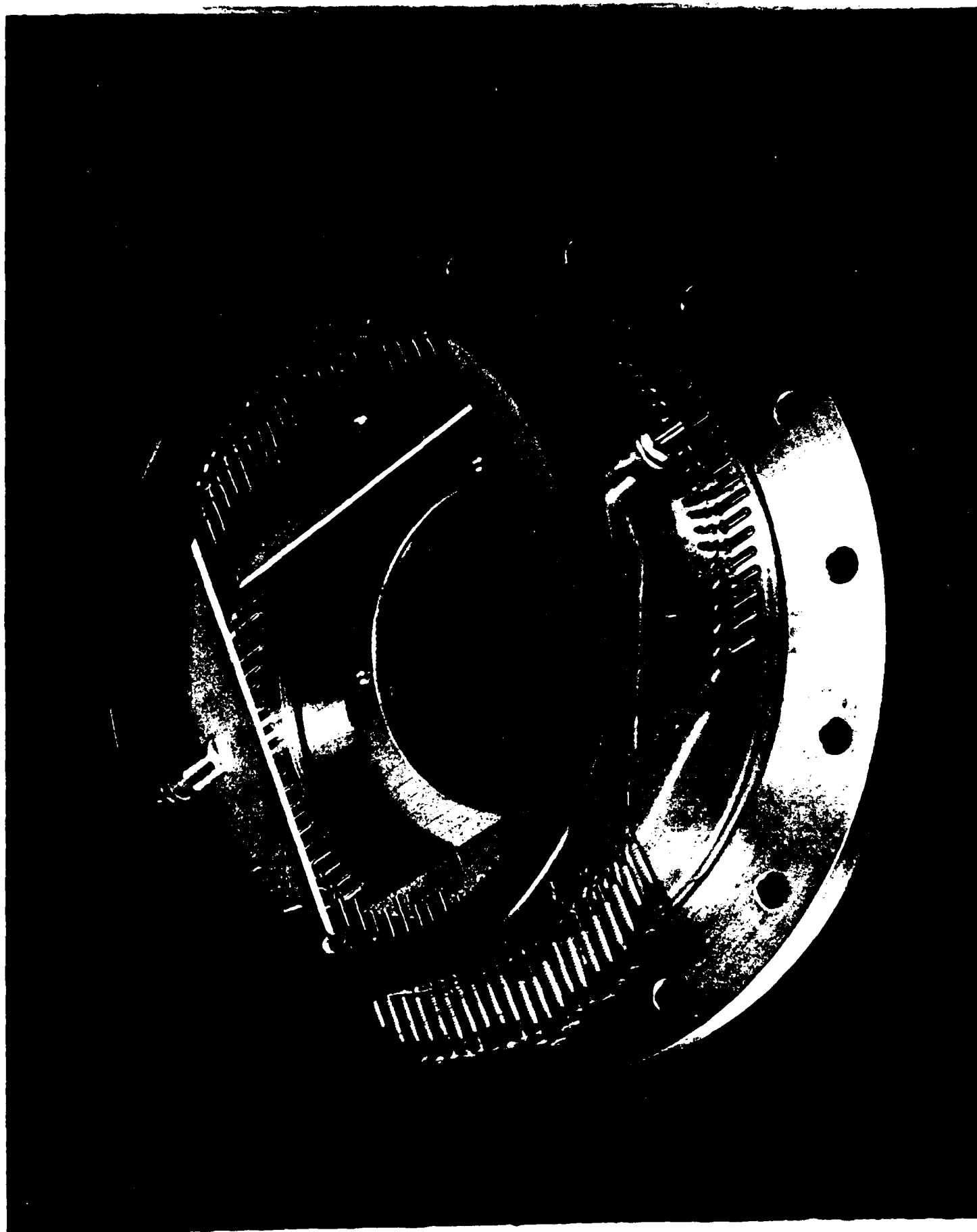
Photographs of Experimental Apparatus

1. Original beam optics test stand with grid focusing experiment and extended drift tube.
2. Close-up view of the grid-focusing apparatus.
3. Upgraded space charge lens experiment.
4. View down the axis of the space-charge lens experiment, illuminated by the electron source. Diagnostic carrier and supports at the center.

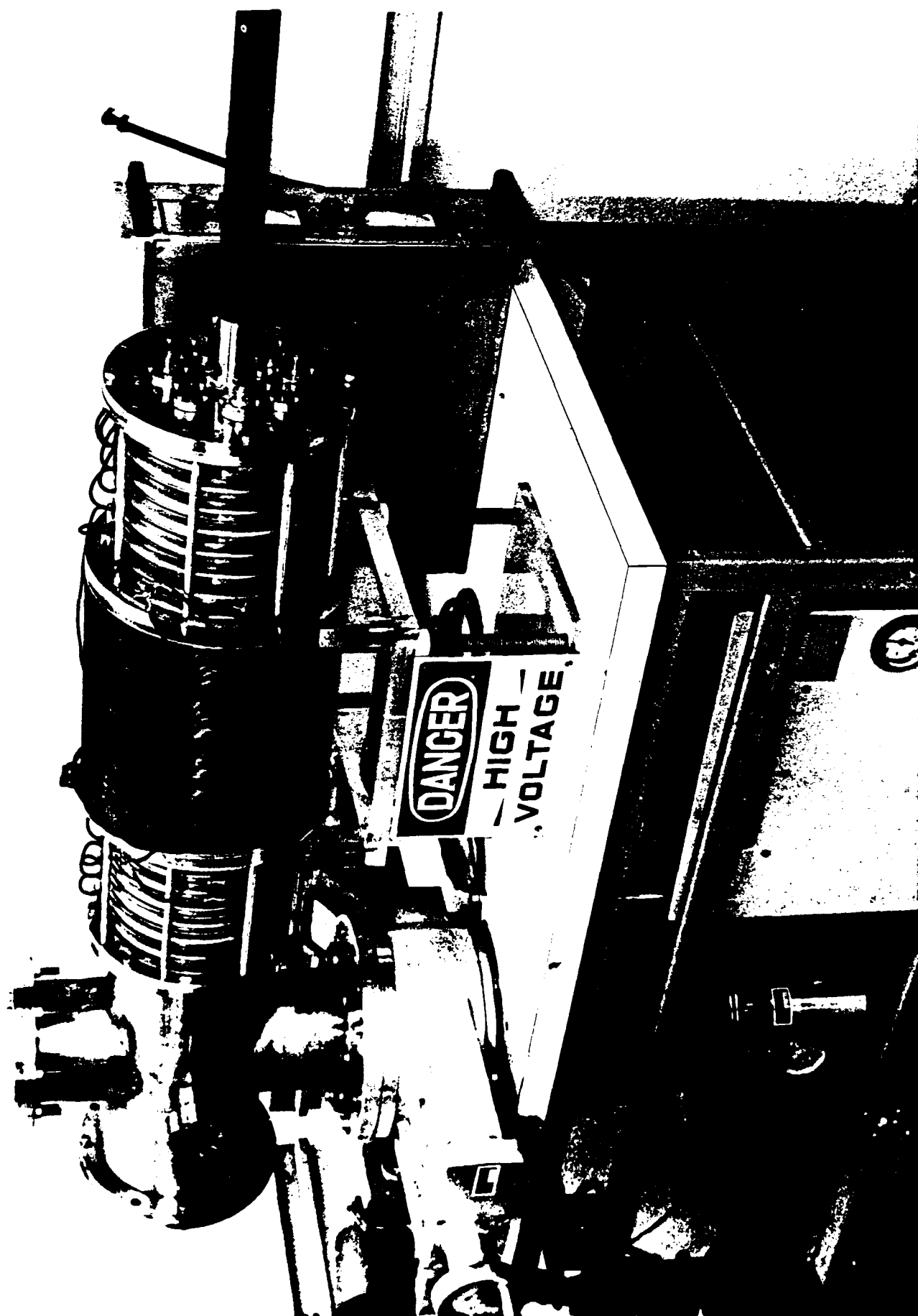
Photograph 01



Photograph 02



Photograph 03



Photograph 04

